# Climatic Impacts of Parameterized Local and Remote Tidal Mixing

ANGÉLIQUE MELET AND SONYA LEGG

*Princeton University, and NOAA/Geophysical Fluid Dynamics Laboratory, Princeton, New Jersey*

ROBERT HALLBERG

*NOAA/Geophysical Fluid Dynamics Laboratory, Princeton, New Jersey*

(Manuscript received 24 February 2015, in final form 1 December 2015)

ABSTRACT

Turbulent mixing driven by breaking internal tides plays a primary role in the meridional overturning and oceanic heat budget. Most current climate models explicitly parameterize only the local dissipation of internal tides at the generation sites, representing the remote dissipation of low-mode internal tides that propagate away through a uniform background diffusivity. In this study, a simple energetically consistent parameterization of the low-mode internal-tide dissipation is derived and implemented in the Geophysical Fluid Dynamics Laboratory Earth System Model with GOLD component (GFDL-ESM2G). The impact of remote and local internal-tide dissipation on the ocean state is examined using a series of simulations with the same total amount of energy input for mixing, but with different scalings of the vertical profile of dissipation with the stratification and with different idealized scenarios for the distribution of the low-mode internal-tide energy dissipation: uniformly over ocean basins, continental slopes, or continental shelves. In these idealized scenarios, the ocean state, including the meridional overturning circulation, ocean ventilation, main thermocline thickness, and ocean heat uptake, is particularly sensitive to the vertical distribution of mixing by breaking low-mode internal tides. Less sensitivity is found to the horizontal distribution of mixing, provided that distribution is in the open ocean. Mixing on coastal shelves only impacts the large-scale circulation and water mass properties where it modifies water masses originating on shelves. More complete descriptions of the distribution of the remote part of internal-tide-driven mixing, particularly in the vertical and relative to water mass formation regions, are therefore required to fully parameterize ocean turbulent mixing.

## 1. Introduction

Turbulent mixing plays a key role in determining the ventilation of the ocean as well as the ocean uptake and storage of heat and carbon (e.g., Bryan 1987; Park and Bryan 2000; Sokolov et al. 2003; Gnanadesikan et al. 2003, 2004; Wunsch and Ferrari 2004) for the equilibrium climate state and for transient climate such as climate change (Dalan et al. 2005; Schiermeier 2007). Away from the boundaries, breaking internal waves are the main driver of diapycnal mixing and provide the mechanical energy necessary to drive a downward transport of heat and turbulently warm the waters so that they upwell and maintain the abyssal stratification and global meridional overturning circulation (Munk and Wunsch 1998). Global amplitudes and patterns of mixing are hence set by the detailed geography of internal-wave generation, propagation, and breaking.

Winds and tides supply energy to the internal-wave field of about 0.5 TW (D'Asaro 1985; Alford 2001, 2003) and 1 TW (Egbert and Ray 2000; Simmons et al. 2004a; Nycander 2005; Melet et al. 2013b), respectively, with an additional 0.2–0.4 TW provided by the interaction of geostrophic flows with rough topography (Nikurashin and Ferrari 2011; Scott et al. 2011). Our focus here is on the internal waves generated by tidal flow over rough topography (Garrett and Kunze 2007). While considerable progress has been made regarding the generation of internal tides, where they ultimately break and dissipate their energy through shear or convective instability remains poorly known. Radiated internal waves cover a large spectrum of wavenumbers. High-mode waves, with slower group velocity, higher shear, and faster wave–wave interactions, are more likely to dissipate close to their generation site (the local or near-field dissipation)

*Corresponding author address*: Angélique Melet, Princeton University, NOAA/Geophysical Fluid Dynamics Laboratory, 201 Forrestal Rd., Princeton, NJ 08540-6649.
E-mail: angelique.melet@noaa.gov

DOI: 10.1175/JCLI-D-15-0153.1

(Klymak et al. 2010), leading to localized bottom-intensified diffusivities over regions of rough topography such as seamounts (Lueck and Mudge 1997; Toole et al. 1997; Carter et al. 2006), ridges (Polzin et al. 1997; Althaus et al. 2003; Aucan et al. 2006; Klymak et al. 2008), canyons, and fracture zones (Ferron et al. 1998; Carter and Gregg 2002; Thurnherr et al. 2005; MacKinnon et al. 2008). In most places, the bulk of the internal-wave energy flux radiates away from its source as low-mode internal waves (leading to remote or far-field dissipation) (Lefauve et al. 2015). Low-mode internal tides radiating thousands of kilometers from their generation sites have been identified in altimetric observations (e.g., Ray and Mitchum 1997; Kantha and Tierney 1997; Egbert and Ray 2000; Cummins et al. 2001; Dushaw 2002; Zhao et al. 2012) and in situ observations (e.g., Morozov 1995; Althaus et al. 2003; Rainville and Pinkel 2006; Lee et al. 2006), as well as in global baroclinic tide models (e.g., Simmons et al. 2004a; Arbic et al. 2010).

There are a variety of processes leading to the dissipation of low-mode internal waves; this dissipation can occur close to the ocean bottom, close to the surface, or in the ocean interior. As they propagate in the ocean basins, low-mode internal-wave energy can cascade to higher modes and, ultimately, to the smallest-scale waves that break, through wave–wave interactions (Polzin 2004; MacKinnon and Winters 2005), topographic reflection and scattering (Müller and Xu 1992; Johnston and Merrifield 2003; Legg 2014), and reflection at the ocean surface (Althaus et al. 2003). The low-mode internal waves that have not been dissipated in the basins ultimately encounter continental slopes and shelves. Evidence has been found for low-mode internal tides breaking on continental slopes (Moum et al. 2002; Nash et al. 2004, 2007; Martini et al. 2011; Klymak et al. 2011; Nash et al. 2012) and in shelf-slope canyons (Carter and Gregg 2002; Jachec et al. 2006; Lee et al. 2009; Gregg et al. 2011; Kunze et al. 2012). By comparing depth-integrated dissipation rates inferred from in situ measurements to maps of the energy input into internal waves with various scenarios for its spatial dissipation, Waterhouse et al. (2014) infer from existing datasets that much (~40%) of the low-mode internal-wave energy dissipation occurs on the continental slopes or in shelf-slope canyons. However, the exact partition of the dissipation and fate of the low modes remains largely unknown.

Diapycnal mixing is intermittent and highly heterogeneous in the horizontal and vertical, reflecting the variability of internal-wave generation and dissipation. Internal-wave breaking occurs on the $O(1–10)$ m scales of finescale shear that leads to instability and mixing. Breaking internal waves therefore occur on scales too small for global ocean models to explicitly resolve, and have to be parameterized to achieve realistic simulations of the ocean and climate. In most recent ocean general circulation models (OGCMs) or climate models, only the local dissipation of internal tides is parameterized, often using the scheme formulated by St. Laurent et al. (2002). Although this scheme uses a physical estimate of the energy flux into the internal-tide field, the spatial distribution of the dissipation is crudely represented by specifying a fixed and uniform fraction of local dissipation with an exponential decay in the vertical (e.g., Simmons et al. 2004b; Saenko and Merryfield 2005; Jayne 2009). Melet et al. (2013a) show that large-scale simulations are sensitive to refinement of this vertical profile to the more physically motivated scheme proposed by Polzin (2009), but a full parameterization of the spatial and temporal variability of the local dissipation fraction is yet to be developed. Recently, some progress has been made to include parameterizations of other internal-wave-driven mixing processes such as the local dissipation of lee waves (Melet et al. 2014) or the dissipation of eddies in the western boundaries of the ocean (Saenko et al. 2012). However, the low-mode energy that is dissipated remotely is not explicitly parameterized in OGCMs and climate models, but is instead accounted for through an ad hoc background diapycnal diffusivity [using for instance a constant value, a latitude-dependent value (Henyey et al. 1986; Harrison and Hallberg 2008), or a stratification-dependent value (Gargett and Holloway 1984)]. An exception is the recent work by Oka and Niwa (2013), in which remotely breaking internal tides have been parameterized in a OGCM in a simple way, assuming a vertically uniform dissipation. Explicitly taking into account the remote dissipation of internal tides in their simulations had a strong impact on the ventilation of the deep Pacific Ocean, with consequences for the ocean carbon cycle. Other modeling studies have shown that the spatial variations of mixing can be important for the ocean state (e.g., Scott and Marotzke 2002; Simmons et al. 2004b; Melet et al. 2013a, 2014). Another attempt to parameterize all topography-induced mixing, including both remote and local internal-wave-driven mixing, is the empirical scheme of Decloedt and Luther (2010), which relates the energy dissipation to a simple roughness metric. However, their parameterization does not account for processes leading to the dissipation of internal waves away from rough topography, and is not energetically constrained. Yet, credible simulations of a changing climate need internal-wave-driven mixing to be represented by energetically constrained and physically based parameterizations to allow mixing to evolve in space and time depending on the ocean state (see Huang 1999).

In this study, we take a step toward a full parameterization of all the internal-tide-driven mixing by deriving a simple energetically consistent parameterization of the low-mode internal-tide dissipation (section 2) and implementing this scheme in a climate model. The impact of low-mode (remote) and local internal-tide dissipation on the climate is examined using different idealized scenarios for the location of the low-mode internal-tide energy dissipation (in the ocean basins, on continental slopes, on continental shelves, or locally at the generation site). A key conclusion is that the same total energy input to mixing can lead to different ocean states, depending on the spatial distribution of that mixing. The vertical distribution of mixing is more important than the horizontal distribution in determining the ocean response. In particular, a vertical distribution in which dissipation is proportional to the buoyancy frequency, so that diffusion is inversely proportional to buoyancy frequency, leads to a sharper thermocline, reduced oceanic heat uptake, and lower thermosteric sea level than the commonly used constant background diffusivity. A vertical profile of dissipation proportional to the squared buoyancy frequency leads to a broader thermocline, more upper-ocean heat uptake, and higher thermosteric sea level, because diffusivity is increased in shallow water and reduced in deep water, relative to the constant diffusivity control. The horizontal location of mixing influences circulation only if it impacts the properties of dense waters in deep water formation regions (i.e., the boundaries of the North Atlantic and the Antarctic). Increased mixing in these regions leads to less dense deep waters, and reduced deep overturning. By contrast, increased mixing in the abyssal ocean tends to enhance deep overturning.

## 2. Model

We performed a series of climate simulations using the GFDL-ESM2G, a global coupled carbon–climate Earth system model (coupled ocean–ice–atmosphere–land–biogeochemistry coupled model), used for the IPCC Fifth Assessment Report (AR5) model suite (Dunne et al. 2012). The ocean model is the Generalized Ocean Layer Dynamics (GOLD) isopycnal model (Hallberg and Adcroft 2009). The zonal resolution is 1° longitude. The meridional resolution is 1° in the midlatitudes from 20° to 60° latitude in both hemispheres, and it increases to ½° poleward of 60° and to ⅓° equatorward of 20°. The model has 63 vertical layers, of which 59 are in the ocean interior. The mixed layer model [a refined bulk mixed layer formulation, as described in Hallberg (2003)] uses two layers, and two additional buffer layers ensure smooth water mass exchange with the isopycnal interior. The isopycnal coordinates allow the interior ocean to be handled more naturally than other vertical coordinates systems (such as $z$ or terrain-following coordinates), and diapycnal mixing is explicitly parameterized, without spurious diapycnal mixing arising from advection as in $z$-coordinate models (Griffies et al. 2000; Ilicak et al. 2012). Thus, the isopycnal coordinates provide a favorable framework for studying the effects of changing the diapycnal mixing. Along-isopycnal tracer mixing occurs via a Laplacian diffusion operator, while the horizontal viscosity uses a combination of Laplacian and biharmonic operators.

Initial conditions correspond to the end of a 1000-yr spinup of GFDL-ESM2G. The spinup starts from the Levitus climatology and uses 1860 radiative forcings and concentrations of aerosols, carbon dioxide, and other radiatively active gases. During the spinup, only the local dissipation of the oceanic internal tide is parameterized according to the St. Laurent et al. (2002) scheme (with a fraction of local dissipation of one-third), and an additional ad hoc diffusivity is added loosely based on the dissipation scheme proposed by Gargett and Holloway (1984):

$$\epsilon_G = 1.0 \times 10^{-7}\,\mathrm{W\,m^{-3}} + 6.0 \times 10^{-4}\,\mathrm{J\,m^{-3}} \times N, \qquad (1)$$

where $N$ is the buoyancy frequency.

In addition to mixing due to the dissipation of internal tides, different parameterizations account for other diapycnal mixing mechanisms in the model. Shear-driven mixing is accounted for by a Richardson number–dependent parameterization (Jackson et al. 2008). The bottom boundary layer is mixed using the parameterization of Legg et al. (2006), and geothermal heating is included based on Adcroft et al. (2001). Finally, a background diapycnal diffusivity is added to account for other sources of mixing that are not otherwise parameterized, such as the dissipation of near-inertial waves. This background diapycnal diffusivity is prescribed using a latitude-dependent profile taking a minimum value of $2 \times 10^{-6}\,\mathrm{m^2\,s^{-1}}$ at the equator and a value of $2 \times 10^{-5}\,\mathrm{m^2\,s^{-1}}$ at 30°N and 30°S (Harrison and Hallberg 2008), following the latitudinal variations in diffusivity shown by Henyey et al. (1986) and Gregg et al. (2003). Mixing due to internal lee waves is not included here, despite recent advances in parameterization (Melet et al. 2014), because our goal is to focus on the far-field internal-tide parameterization in isolation.

Diapycnal viscosity is inferred from diapycnal diffusion using a unit Prandtl number. A background kinematic viscosity of $10^{-4}\,\mathrm{m^2\,s^{-1}}$ and additional parameterizations are used for the diapycnal viscosity (notably in the

bottom boundary layer and surface mixed layer) so that the Prandtl number is actually always greater than 1.

This 1000-yr spinup run, including the choices of diffusion parameterizations and the 1860 forcing, is documented as the preindustrial control run in the model suite from phase 5 of CMIP (CMIP5) of simulations described in Dunne et al. (2012). We use this as the starting point for our experiments because the climate generated by this setup is reasonably realistic, while our goal here is to understand the impact of different distributions of tidal mixing, so as to develop better physically based parameterizations of interior diffusivity constrained by the tidal energy budget.

### a. *Internal-tide-driven mixing parameterizations*

#### 1) Energy flux into internal tides

The energy flux per unit area into internal tides $E_T$ is diagnosed online using the scale relation of Jayne and St. Laurent (2001), which is consistent with internal-tide generation theoretical studies (Bell 1975):

$$E_T(x,y,t) = \frac{1}{2}\rho_0 N_b \kappa h^2 \langle U^2 \rangle . \tag{2}$$

Here, $N_b$ is the buoyancy frequency along the seafloor, $\langle U^2 \rangle$ is the barotropic tide variance [barotropic tidal velocities are computed with eight major tidal components by the Oregon State University tidal model (Egbert and Erofeeva 2002)], and $\kappa$ and $h$ are the wavenumber and amplitude scales for the topographic roughness, respectively. The topographic roughness $h^2$ is computed as the root-mean-square height deviations from a least squares fit of the topography to a plane over a grid box using the Smith and Sandwell (1997) bathymetric dataset. We use $\kappa$ as a characteristic inverse length scale of topography, which is treated as a spatially uniform free parameter set here to $2\pi/(16\,\text{km})$. In our simulations, the resulting globally integrated energy flux into internal tides is 1.0 TW. Equation (2) assumes linear internal waves generated at small-amplitude subcritical topography, and is inaccurate at tall steep ridges.

#### 2) Local dissipation of internal tides

The local dissipation of internal-tide energy is parameterized following the commonly used semiempirical scheme proposed by St. Laurent et al. (2002), for simplicity. In this parameterization, first implemented in an OGCM by Simmons et al. (2004b) and subsequently by many others (e.g., Saenko and Merryfield 2005; Bessières et al. 2008; Jayne 2009), the turbulent dissipation rate of internal-tide energy $\epsilon$ is expressed as

$$\epsilon_L = \frac{q_L E_T(x,y,t)}{\rho} F_L(z), \tag{3}$$

with $\rho$ the density of seawater, $E_T(x,y,t)$ the energy flux per unit area transferred from barotropic to internal tides, and $q_L$ the fraction of internal-tide energy dissipated locally. In this study, as in St. Laurent et al. (2002), we use a constant value for $q_L$. In fact, observational (Waterhouse et al. 2014; Falahat et al. 2014), numerical (Nikurashin and Legg 2011; Klymak et al. 2010), and theoretical (Lefauve et al. 2015) studies have shown that $q_L$ should be a function of space and time. In particular, regions of small-scale rough topography are likely to have $q_L$ values approaching unity, particularly equatorward of the critical latitude for nonlinear wave–wave interactions, while regions of large ridge topography are likely to have low values of $q_L$ with much of the energy propagating away as low-mode internal tides.

The vertical structure of dissipation in the St. Laurent et al. (2002) formulation $F_L(z)$ corresponds to an exponential function that satisfies energy conservation within an integrated vertical column (i.e., its integral over depth equals one):

$$F_L(z) = \frac{e^{-z/z_s}}{z_s(1-e^{-H/z_s})}, \tag{4}$$

with $z$ the height above the seafloor; $z_s$ a constant decay scale, set to 300 m in GFDL-ESM2G (Dunne et al. 2012); and $H$ the total ocean depth.

A more physically based vertical profile of the local energy dissipation of internal tides has been formulated by Polzin (2009), and Melet et al. (2013a) show that the vertical distribution of the dissipation of internal-wave energy matters for the ocean state and should therefore evolve in time and space with the ocean state. However, in this study we chose to use the simpler semiempirical scheme of St. Laurent et al. (2002). We do not intend to examine the most realistic case for the energy dissipation of internal waves, but rather to examine the impact of the addition of low-mode wave energy dissipation and its spatial distribution on the ocean state in a climate model.

#### 3) Remote dissipation of internal tides

In this study, the remote dissipation of the remaining internal-tide energy can occur on continental slopes, continental shelves, and in the ocean basins. Continental slopes were defined as regions where the model bathymetry exhibits slopes larger than 0.01. Ocean basins were defined as regions deeper than 500 m, outside the continental slopes. Continental shelves were defined as the remaining ocean points.

Finally, a cutoff latitude of 74.5°, corresponding to the $M_2$ critical latitude, was used and microtidal seas (i.e., the Black, Red, Mediterranean, and Baltic Seas; the Persian Gulf; and Hudson Bay, where barotropic tides have low amplitudes) were excluded, as is the Arctic Ocean (white regions in Fig. 1b). Local dissipation of internal tides is however still possible in the above regions excluded from remote mixing, although the low amplitude of barotropic tides does not generally allow the generation of energetic internal tides (see Melet et al. 2014, their Fig. 1). The model bathymetry and the corresponding masks for continental slopes, continental shelves, and ocean basins are shown in Fig. 1.

The internal-tide energy that is not dissipated locally according to (3) is dissipated remotely on continental slopes $\epsilon_S$, ocean basins $\epsilon_B$, or continental shelves $\epsilon_C$ following the St. Laurent et al. (2002) template:

$$\epsilon_r = \frac{E_r(t)}{\rho} F_r(z), \tag{5}$$

with subscript $r = C$, $S$, or $B$ representing variables for continental shelves, continental slopes, and ocean basins, respectively, and $F_r(z)$ being the vertical structure of dissipation for the low mode, satisfying energy conservation within an integrated vertical column. Here, $E_S(t)$, $E_C(t)$, and $E_B(t)$ are the energy flux amplitudes of the waves at continental slopes, continental shelves, and in the ocean basins, respectively. These energy flux amplitudes are prescribed to be spatially uniform, without considering the dynamics of any particular region or how low modes are distributed along beams or attenuated:

$$E_r(t) = \frac{q_r E_{T,\mathrm{global}}(t)}{A_r}, \tag{6}$$

where $E_{T,\mathrm{global}}$ is the energy flux into internal tides integrated globally and $A_S$, $A_C$, and $A_B$ are the areas covered by continental slopes, continental shelves, and ocean basins, respectively (Fig. 1b). In (6), $q_S$, $q_C$, and $q_B$ are the fraction of internal-tide energy dissipated on continental slopes, on continental shelves, and in ocean basins, respectively, with

$$q_L + q_S + q_B + q_C = 1. \tag{7}$$

Therefore, all the energy into internal tides is dissipated over the global ocean in our simulations.

A choice must be made for the vertical structure of the dissipation of the low-mode internal tides. We will consider different vertical profiles in this study:

- scaling 1—$\epsilon_r$ scales with $F_L(z)$, that is, an exponential decrease above the seafloor;
- scaling 2—$\epsilon_r$ scales with $N$; and
- scaling 3—$\epsilon_r$ scales with $N^2$.

The first scaling of the dissipation profile is stratification independent and is identical to that used for the local dissipation in (3) and (4). This profile is motivated by the bottom-intensified dissipation simulated at critical slopes (Legg 2014). In this study this profile will only be applied over continental slopes. However, no restriction will be made to critical slopes; this profile will be applied to all continental slopes, regardless of steepness.

The second scaling corresponds to the vertical structure suggested by Gargett (1984). Gargett and Holloway (1984) also presented a parameterization of diapycnal mixing due to internal-wave breaking in which $\epsilon = aN + b$, where $a$ and $b$ are empirically determined constants, implemented as an ad hoc parameterization in standard versions of GFDL-ESM2G, such as the one used for the IPCC AR5 model suite (Dunne et al. 2012). In this scaling, the dissipation scales with internal-wave energy, which scales with the buoyancy frequency when vertically varying stratification is taken into account in internal-wave linear theory (Gill 1982, section 8.12). A more physical justification of this parameterization comes from numerical simulations of catastrophic breaking of low-mode waves, when the energy is transferred from the low-mode wave to turbulence scales without passing through a gradual cascade. Examples include catastrophic parametric subharmonic instability at the critical latitude (MacKinnon and Winters 2005) (appropriate for dissipation in the basins) and shoaling at continental slopes (Legg 2014). However, no observational evidence yet exists to support such a scaling of dissipation with internal-wave energy and hence buoyancy frequency.

The third scaling corresponds to the consensus from observations of the relationship between dissipation and stratification in the open ocean away from rough topography (Waterhouse et al. 2014). This relationship is supported by wave–wave interaction theory, which indicates a scaling of dissipation rates with the squared energy of internal waves (e.g., McComas and Müller 1981; Henyey et al. 1986; Gregg 1989; Polzin et al. 1995). This scaling is therefore most appropriate to the deep basins, with less supporting observational evidence over continental slopes.

The stratification dependence of the dissipation in the second and third scalings means that the remote

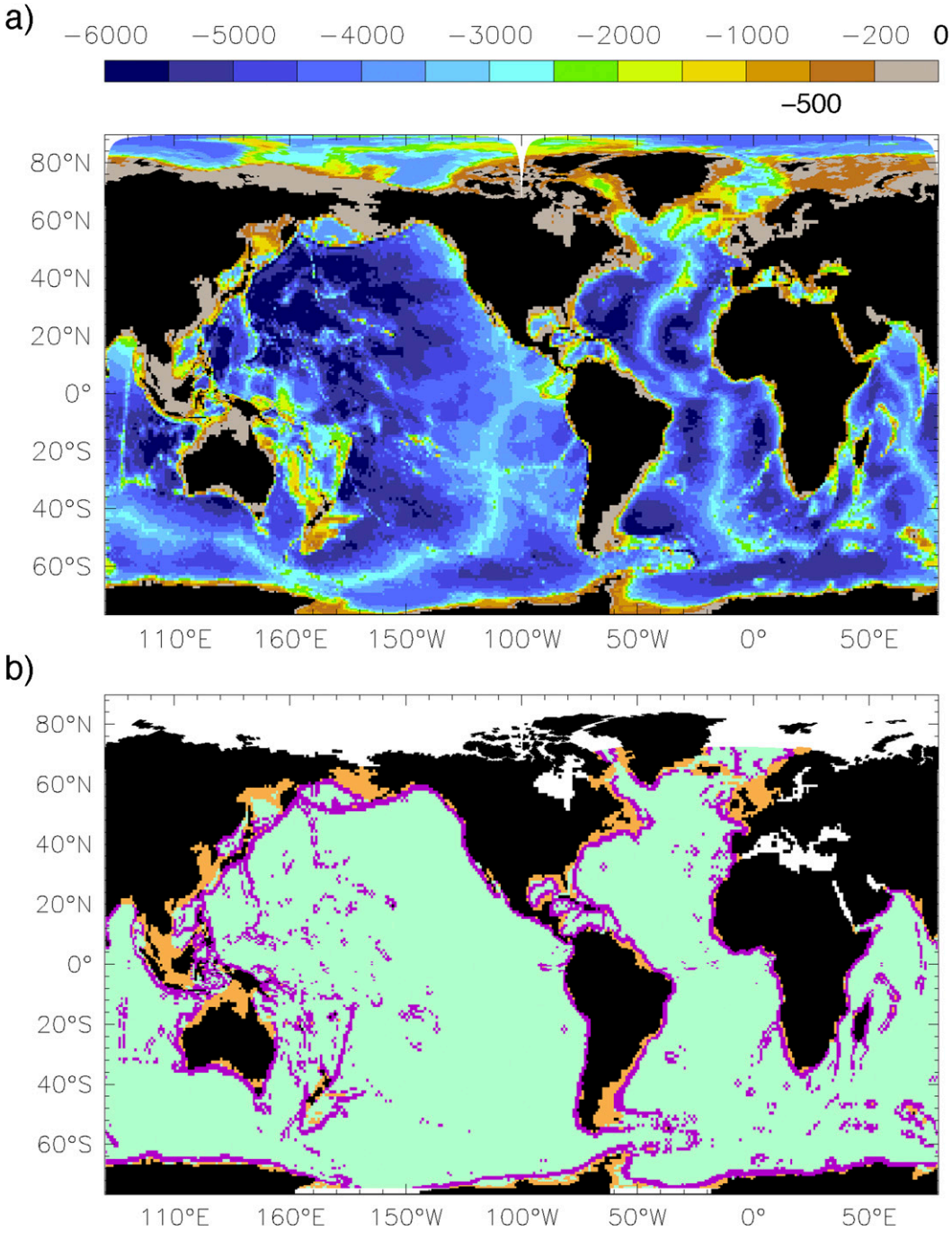


FIG. 1. (a) Model bathymetry (m) and (b) masks used for continental shelves (orange), continental slopes (purple), and ocean basins (cyan) for the remote dissipation of low-mode internal tides. White regions were excluded from the definition of the masks for continental slopes, continental shelves, and ocean basins. Only the local dissipation of internal tides is therefore prescribed in those regions for the S80N, S80N$^2$, S80exp, B80N, B80N$^2$, and C80N experiments (see Table 1).

energy dissipation of internal tides will be stronger in the thermocline in scaling 2 and even more so in scaling 3. The vertical structures of scalings 2 and 3 are finally normalized so that energy is conserved within an integrated vertical column, which requires dividing by the local ocean depth $H$. Therefore, the dissipation of low-mode internal tides is parameterized as follows:

TABLE 1. List of the numerical experiments. The names of the experiments are listed with their corresponding $q_L$, $q_S$, $q_B$, and $q_C$ (see Fig. 1b for areas defined as continental slopes, ocean basins, and continental shelves); and $F(z)$ describes the choice of vertical profile for the internal-tide energy dissipation. The local dissipation of internal tides is exponentially decaying from the ocean bottom. For S80N, B80N, and C80N, the remote dissipation of low-mode internal tides is prescribed using a profile proportional to the buoyancy frequency, while in S80N$^2$ and B80N$^2$, the dissipation profile scales like the square of the buoyancy frequency. In S80exp, the remote dissipation of low-mode internal tides is prescribed using an exponentially decaying profile similar to that of local dissipation.

| Expt | $q_L$ (%) | $q_S$ (%) | $q_B$ (%) | $q_C$ (%) | $F(z)$ |
|---|---|---|---|---|---|
| NoIW | 0 | 0 | 0 | 0 | — |
| L20 | 20 | 0 | 0 | 0 | Exponentially decaying. |
| L100 | 100 | 0 | 0 | 0 | Exponentially decaying. |
| KdLMcst | 20 | — | — | — | $Kd_{LM}$ for remote mixing is constant with depth. |
| S80exp | 20 | 80 | 0 | 0 | Exponentially decaying. |
| S80N | 20 | 80 | 0 | 0 | Remote mixing scales with $N$. |
| S80N$^2$ | 20 | 80 | 0 | 0 | Remote mixing scales with $N^2$. |
| B80N | 20 | 0 | 80 | 0 | Remote mixing scales with $N$. |
| B80N$^2$ | 20 | 0 | 80 | 0 | Remote mixing scales with $N^2$. |
| C80N | 20 | 0 | 0 | 80 | Remote mixing scales with $N$. |

- scaling 1,

$$\epsilon_r = \frac{q_r}{\rho}\frac{E_{T,\mathrm{global}}(t)}{A_r}\frac{e^{-z/z_s}}{z_s(1-e^{-H/z_s})}; \tag{8}$$

- scaling 2,

$$\epsilon_r = \frac{q_r}{\rho}\frac{E_{T,\mathrm{global}}(t)}{A_r}\frac{1}{H}\frac{N}{\overline{N}}; \quad \text{and} \tag{9}$$

- scaling 3,

$$\epsilon_r = \frac{q_r}{\rho}\frac{E_{T,\mathrm{global}}(t)}{A_r}\frac{1}{H}\frac{N^2}{\overline{N^2}}. \tag{10}$$

The overbars in (9) and (10) denote a vertical average.

Finally, spatially and temporally varying turbulent diffusivities are inferred from the dissipation using the Osborn (1980) model:

$$K_d = \frac{\Gamma\epsilon}{N^2}. \tag{11}$$

Here, $\Gamma$ is related to the mixing efficiency of turbulence and is generally set to $\Gamma = 0.2$ (see e.g., Oakey (1982) and St. Laurent and Schmitt (1999) for justification of this choice). However, to deal with very weak stratification where vertical buoyancy fluxes cannot be sustained and $\Gamma$ should be much smaller than 0.2, we replaced $\Gamma = 0.2$ in our model by

$$\Gamma = 0.2\frac{N^2}{N^2+\Omega^2}, \tag{12}$$

where $\Omega$ is the angular velocity of Earth, as in Melet et al. (2013a). This formulation captures the reduction of $\Gamma$ toward zero for very weak stratification, thereby eliminating spuriously large diffusivities that might otherwise occur in weakly stratified regions. More physically based representations of the dependence of $\Gamma$ on stratification are the subject of ongoing research (Bouffard and Boegman 2013; de Lavergne et al. 2015b).

From (11) we see that with scaling 2, diffusivity will be inversely proportional to $N$, while in scaling 3, diffusivity will be independent of both stratification and vertical location, but inversely proportional to total depth. Hence, in scaling 3, regions of shallow depth will have larger diffusivity than deeper regions of the ocean.

### b. Numerical experiments

A suite of simulations from the GFDL-ESM2G has been performed to study the impact of the dissipation of low-mode internal tides on the climate. Simulations were run for 1000 yr using the preindustrial forcing of 1860. Different scenarios for the fractions of internal-tide local energy dissipation and remote dissipation in the ocean basins, on continental slopes and shelves, have been considered. The 10 simulations analyzed in the present study are described below (a summary is provided in Table 1).

Simulations with no explicit parameterization of remote mixing include the following:

- No internal-wave-driven mixing is parameterized (noIW); neither St. Laurent et al. (2002) nor background diffusivity representing tidally driven processes are included.
- Only the local dissipation of internal-tide energy is parameterized, with 20% of the internal-tide energy being dissipated locally (L20), using the St. Laurent et al. (2002) parameterization and exponentially decaying vertical profile; the choice of 20% for the local dissipation is based on results by Waterhouse et al. (2014) and on the example of the energy dissipation at the Hawaiian Ridge (Rudnick et al. 2003; Klymak et al. 2006); Waterhouse et al. (2014) suggests that

20% is likely a lower bound for the fraction of local dissipation.
- Similar to L20, but with 100% of the internal-tide energy being dissipated locally (L100). This experiment corresponds to the extreme case where internal-tide energy is entirely dissipated locally and there is no energy in low-mode internal tides.

Simulations with an explicit parameterization of remote mixing, using 20% of local mixing [with the St. Laurent et al. (2002) scheme] and 80% of remote dissipation include the following:

- The remote dissipation of internal tides is added with a constant and spatially uniform diapycnal diffusivity (KdLMcst). The value of this constant is set so that the work against stratification done by low-mode internal tide dissipation is consistent with the global energy input into low modes,

$$\mathrm{Kd}_{\mathrm{LM}} = \frac{\Gamma(q_S + q_B + q_C)\iint E_T(x,y)\,dx\,dy}{\iiint \rho_0 N^2\,dx\,dy\,dz}. \quad (13)$$

  In our model, this value corresponds to $1.4 \times 10^{-5}\,\mathrm{m^2\,s^{-1}}$. Note that from (11), setting the diffusivity to be constant is equivalent to setting the dissipation proportional to $N^2$.
- Remote dissipation of the internal-tide energy is over continental slopes, using a vertically decaying profile (S80exp, scaling 1).
- Remote dissipation of the internal-tide energy is over continental slopes, using a vertical profile of dissipation scaling with $N$ (S80N, scaling 2).
- Remote dissipation of the internal-tide energy is over continental slopes, using a vertical profile of dissipation scaling with $N^2$ (S80N$^2$, scaling 3).
- Remote dissipation of the internal-tide energy is in ocean basins, using a vertical profile of dissipation scaling with $N$ (B80N, scaling 2).
- Remote dissipation of the internal-tide energy is in ocean basins, using a vertical profile of dissipation scaling with $N^2$ (B80N$^2$, scaling 3).
- Remote dissipation of the internal-tide energy is over continental shelves, using a vertical profile of dissipation scaling with $N$ (C80N, scaling 2).

By definition, experiments S80exp, S80N, S80N$^2$, B80N, B80N$^2$, C80N, KdLMcst, and L100 have the same total magnitude of internal-tide dissipation, while experiments S80exp, S80N, S80N$^2$, B80N, B80N$^2$, C80N, and KdLMcst have the same total magnitude of remote dissipation.

The ad hoc diffusivity based on (1) that was added during the spinup simulation is not added in the simulations analyzed in this study. The background diapycnal diffusivity based on Harrison and Hallberg (2008) is however retained in all simulations to account for other sources of mixing that are not parameterized explicitly.

None of the idealized scenarios considered here are expected to reproduce the geography of low-mode energy dissipation in the real ocean where the fractions of the energy that are dissipated close to the generation site, during the propagation of internal tides in the ocean basins, on the continental slopes and shelves all vary both in time and space. Instead, our goal is to assess the sensitivity of the ocean circulation to the distribution of low-mode internal-tide energy dissipation, for which idealized experiments focusing on one type of spatial distribution in isolation are most useful.

## 3. Results

For most of our results, we will use KdLMcst, in which the low-mode dissipation is represented through a constant background diffusivity, as our reference case. This simulation most closely resembles the implementation of the St. Laurent et al. (2002) parameterization in several CMIP5 models (e.g., GFDL-ESM2G; note however that we are specifying 20% local dissipation, instead of the 30% prescribed in the GFDL-ESM2G CMIP5 simulations). Figure 2 shows that the simulations are not completely equilibrated after 1000 years. Because the spinup run is initialized with present-day observed ocean temperature and salinity but is run with 1860 concentrations of radiatively active gases and aerosols, during the spinup the ocean drifts with a time scale of thousands of years from its initial state into a cooler equilibrium state that is closer to what might have been observed in 1860. Any change in the diffusivities leads to a new equilibrium state and a similarly long adjustment. For example, the drift in KdLMcst relative to the spinup run can be explained by the different fractions of local internal-tide energy dissipation, set to 20% in KdLMcst and to 30% in the spinup run, and by the different ad hoc diffusivities, based on (1) in the spinup and on a constant value in KdLMcst from (13). As a result of this climate drift, the amplitude of the sensitivity of the ocean state to remote dissipation and mixing increases in time, but results for centuries late in the simulation are qualitatively similar. In the following, results are shown for the mean of the last century of the simulations (years 901–1000).

### a. Differences in diffusivity

All differences in the simulations ultimately reflect differences in the magnitude and distribution of diapycnal diffusivity. The zonally averaged diapycnal diffusivity

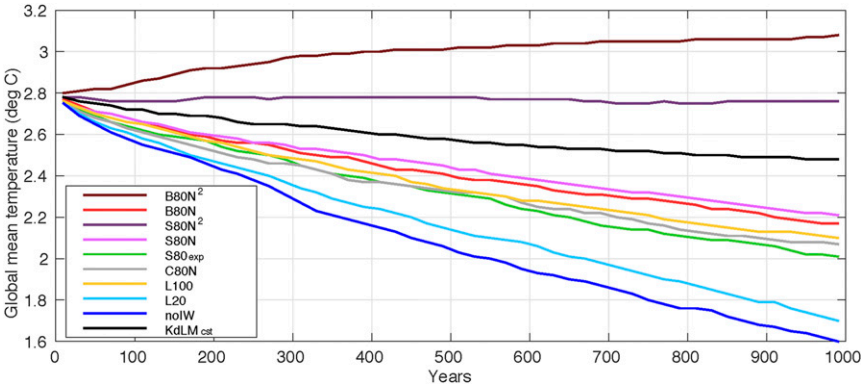


FIG. 2. The globally averaged ocean temperature (°C) for all simulations as a function of simulation time. The spunup control run of GFDL-ESM2G (Dunne et al. 2012) provides the initial conditions at year 0. Increasing the mixing generally warms the ocean, as does shifting the mixing energy into more stratified waters.

due to all parameterized processes, including shear-driven and convective mixing in addition to internal-tide-driven mixing (section 2), is shown in Fig. 3. Diapycnal diffusivity due to internal-tide-driven mixing only is shown in Fig. 4. The importance of diapycnal mixing induced by processes other than internal-tide dissipation can be seen from the noIW experiment in Fig. 4: convective and shear-driven mixing induce diapycnal mixing mostly in the upper ocean and at high latitudes. With only mixing due to internal-tide local dissipation (L20), diffusivity is enhanced in the deep ocean compared to the case with no internal-wave-driven mixing (noIW), and this is further increased for L100, but the diffusivity is still very low in the thermocline.

When remote dissipation is included, different spatial patterns of diffusivity result from the different vertical and horizontal distributions of that dissipation: B80N$^2$, S80N$^2$, B80N, S80N, and KdLMcst have increased mixing in the thermocline relative to L20 and L100. While both B80N and S80N have greater diffusivity at depth than KdLMcst, B80N has greater enhancement at depth than S80N, since dissipation is localized in regions of greater depth in B80N than in S80N (Fig. 1). Conversely, B80N$^2$ and S80N$^2$ have slightly less diffusivity at depth but larger diffusivities in the thermocline than KdLMcst. In B80N$^2$ and S80N$^2$ the diffusivity is locally vertically uniform but depends on the inverse of total depth, so that shallower ocean regions (such as the midocean ridges) have larger diffusivity than deeper ocean regions (such as the abyssal plains). The horizontal averaged diffusivity is therefore greater in the upper ocean, and lower in the deep ocean compared to the constant diffusivity of KdLMcst. In the Southern Ocean, whereas B80N and S80N have diffusivities that increase with depth over the upper 2 km of the ocean as stratification decreases, B80N$^2$ and S80N$^2$ have stratification-independent diffusivity that is larger than B80N and S80N in the upper 500 m and smaller in the rest of the ocean.

C80N contrasts with the other cases with the same total magnitude of dissipation (i.e., B80N$^2$, S80N$^2$, B80N, S80N, and L100). When all the dissipation occurs on shelves, the zonally averaged deep-ocean diffusivities are little changed compared to L20. Differences are seen near the surface at 40°–70°S and 60°–70°N (over the shallow shelves) where diapycnal mixing due to internal waves is enhanced in C80N compared to L20 (Fig. 4). This enhanced mixing over the shelves leads to less dense overflows, which in turn leads to less shear- and bottom-drag-driven mixing, explaining the weaker diapycnal diffusivity, resulting from all parameterized processes, at depth in C80N than in L20 at 60°–70°N. Dissipation over continental slopes, but with an exponentially decaying profile in the vertical (S80exp) results in a diffusivity that closely resembles that of L100, although with slightly greater diffusivity in the thermocline, and slightly less at depth. The resemblance of the L100 and S80exp diapycnal diffusivities is due to the fact that in the S80exp simulation, dissipation is exponentially decaying from the ocean bottom (as in L100), and the locations of slopes (used in S80exp; Fig. 1) partly coincide with locations of internal-tide generation (used in L100).

The globally averaged diffusivity profiles are shown in Fig. 5, as differences from the KdLMcst profile. In the upper thermocline (e.g., 50–200 m), only B80N$^2$ and S80N$^2$ have greater diffusivity than KdLMcst. C80N shows the smallest differences from KdLMcst in this region. In the lower thermocline (300–700 m), C80N, L20, and noIW have less diffusivity than KdLMcst,

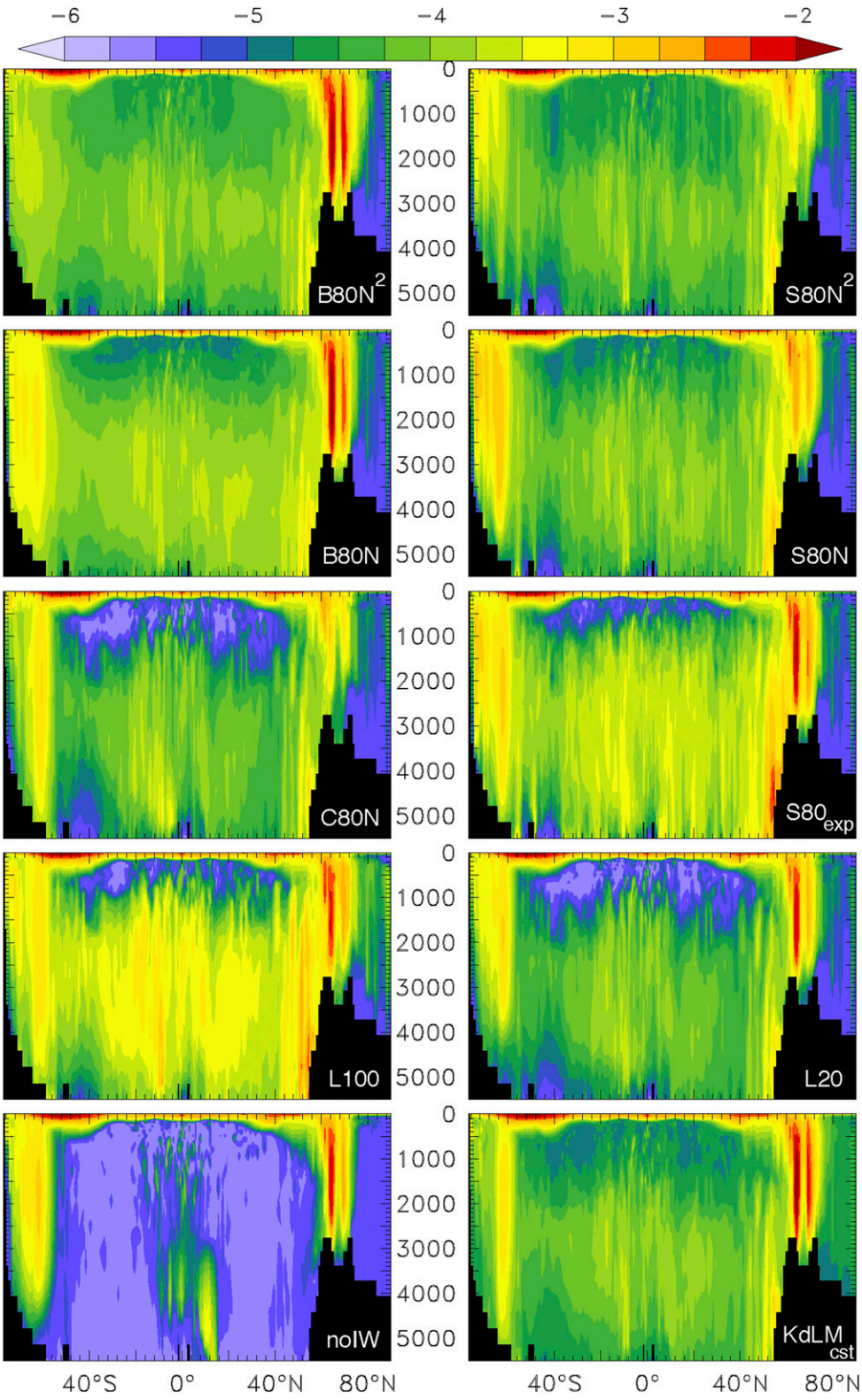


FIG. 3. Global zonal mean of diapycnal diffusivities ($\log_{10} m^2 s^{-1}$) averaged over the last century of the 1000-yr simulations.

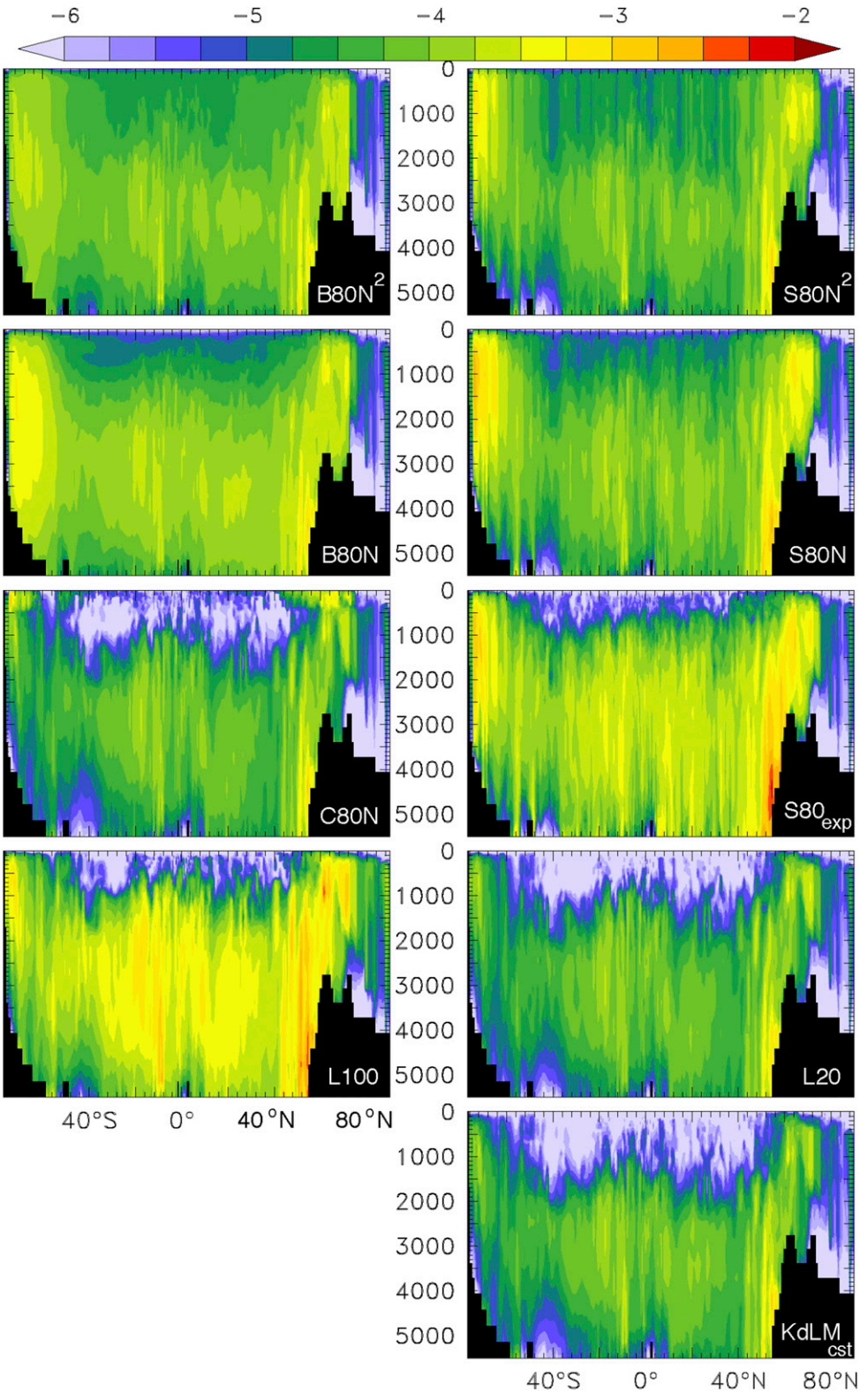


FIG. 4. Global zonal mean of diapycnal diffusivities due to internal-tide mixing parameterizations ($\log_{10}\,m^2\,s^{-1}$) averaged over the last century of the 1000-yr simulations. Note that for KdLMcst, the constant and spatially uniform diapycnal diffusivity of $1.4 \times 10^{-5}\,m^2\,s^{-1}$ has not been added in the bottom-right panel.

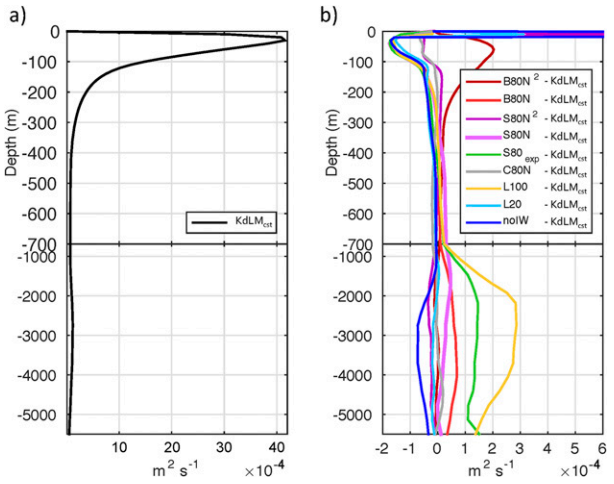


FIG. 5. Vertical profiles of (a) the global-mean diffusivity of the KdLMcst simulation and (b) the global-mean diffusivity of the other simulations shown as a difference from the KdLMcst profile. Note that the large near-surface values seen in (a) are due to convective and shear instabilities and not to tidally driven mixing.

while S80N$^2$, B80N, and L100 are similar to KdLMcst, and B80N$^2$ and S80N have greater diffusivity. At depth, L100 and S80exp have the greatest diffusivity followed by B80N, then S80N, C80N, and B80N$^2$. S80N$^2$, L20, and noIW have the smallest diffusivities at depth.

### b. *Impact of remote diffusivity on temperature and stratification*

The zonally averaged temperature (Fig. 6) reflects the overall differences in diffusivity; smaller diffusivities in the thermocline and above lead to a cooler and thinner thermocline (seen in all simulations but B80N$^2$ and S80N$^2$ compared to KdLMcst), and larger diffusivities at depth lead to a warmer abyss (L100 and S80exp), consistent with the downward diffusion of heat in the stratified ocean. However, ocean water masses are also influenced by the diffusivities near their origin: when remote mixing is over slopes or basins (S80N and B80N), the Antarctic Bottom Water (AABW) is colder compared to KdLMcst, as indicated by the cold anomaly through the whole water column in the far Southern Ocean, and then extending northward in the abyss. By contrast, B80N$^2$ and S80N$^2$ have warmer mode and upper deep water than KdLMcst, consistent with their larger diffusivities in the upper-thermocline region. In B80N$^2$, the deep and abyssal oceans are warmer than KdLMcst perhaps because deep convection is weakened in the Southern Ocean (as is discussed later in section 3c) and heat is diffused downward. Finally, AABW temperatures are little changed compared to KdLMcst for remote mixing on the shelves (C80N) (i.e., there is little temperature difference in the deepest water or in the Southern Ocean). Both C80N and KdLMcst have nonzero remote mixing on Antarctic shelves, which tends to warm the AABW. Neither S80N$^2$ nor B80N$^2$ have mixing on shelves, but they do have large surface diffusivities that perform a similar role in warming the AABW.

As a result of the cooler thermocline relative to KdLMcst seen in all simulations except B80N$^2$ and S80N$^2$, the stratification is stronger in the upper ocean (near 500-m depth) and weaker below the thermocline (from 1000- to 2000-m depth), especially in L100 (Fig. 7). In the upper ocean, stratification differs least from KdLMcst in S80N and B80N consistent with the smaller differences in diffusivity in this region. At depth, S80N and B80N have stronger stratification than KdLMcst, because of the warming of upper deep waters resulting from the inverse dependence of diffusivity on stratification, and the cooling of bottom waters, due to the reduction in diffusion on the shelves. Other simulations show smaller differences from KdLMcst in the deep ocean, primarily an increase in stratification in the northern abyss, seen in low deep mixing simulations such as C80N, L20, and noIW, associated with colder bottom waters in the north. In B80N$^2$ and S80N$^2$, internal-wave energy dissipation occurs higher in the thermocline (Fig. 4). As a result, the stratification is slightly weaker in the thermocline (around 500-m depth) and stronger below the thermocline (from 1000- to 2000-m depth). In these simulations with a diffusivity that is locally independent of depth, the stratification is especially strong in the Southern Ocean upper part of the Circumpolar Deep Water (between 500 and 3000 m) where the isopycnals are tilted. S80exp shows stratification intermediate between S80N and L100, but closer to L100. C80N and L20 have very similar stratification, except in the deep Southern Ocean where L20 has stronger stratification, as a result of colder AABW. Additional mixing on the shelves in C80N does not have much influence on the global stratification except through dilution of the Antarctic Bottom Water.

### c. *Impact of remote diffusivity on the meridional overturning circulation and heat transport*

Global meridional overturning circulation is shown in Fig. 8. Both mean and parameterized eddy-induced overturning are included. The overturning is also shown separately for the Atlantic Ocean (Fig. 9) and the Indo-Pacific region (Fig. 10). In simulations with an exponentially decaying or $N$-scaling dissipation profile, the deep overturning in the Indo-Pacific is enhanced compared to KdLMcst. L100 has a particularly strong deep Pacific overturning, associated with the greatly enhanced deep mixing (Fig. 10). Except for B80N$^2$, all other cases have

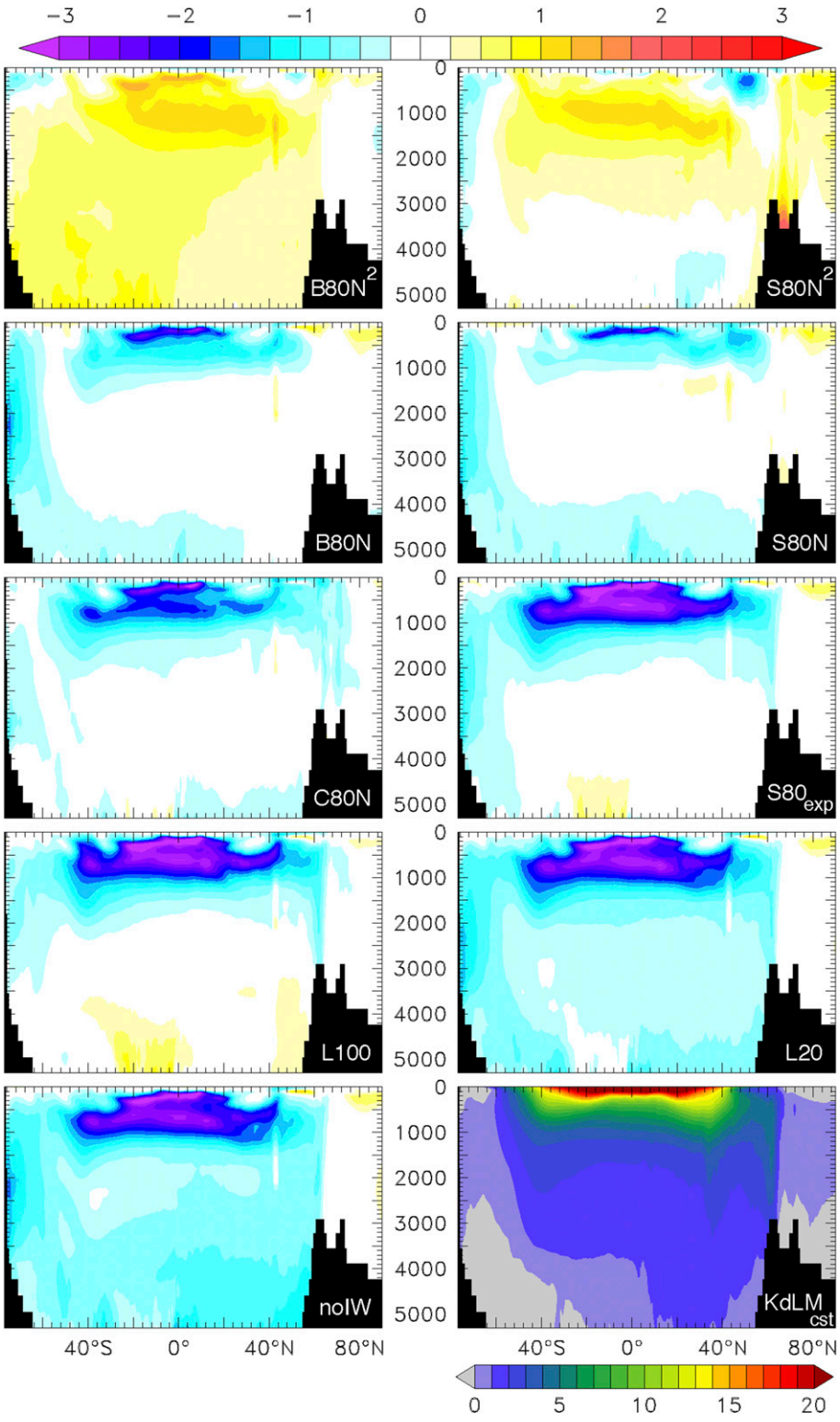


FIG. 6. Global zonal-mean temperature (°C) shown as a temperature difference from the KdLMcst simulation. The color bar is shown across the top. Below the bottom-right panel, the corresponding color bar shows the global zonal-mean temperature (°C) of the KdLMcst simulation.

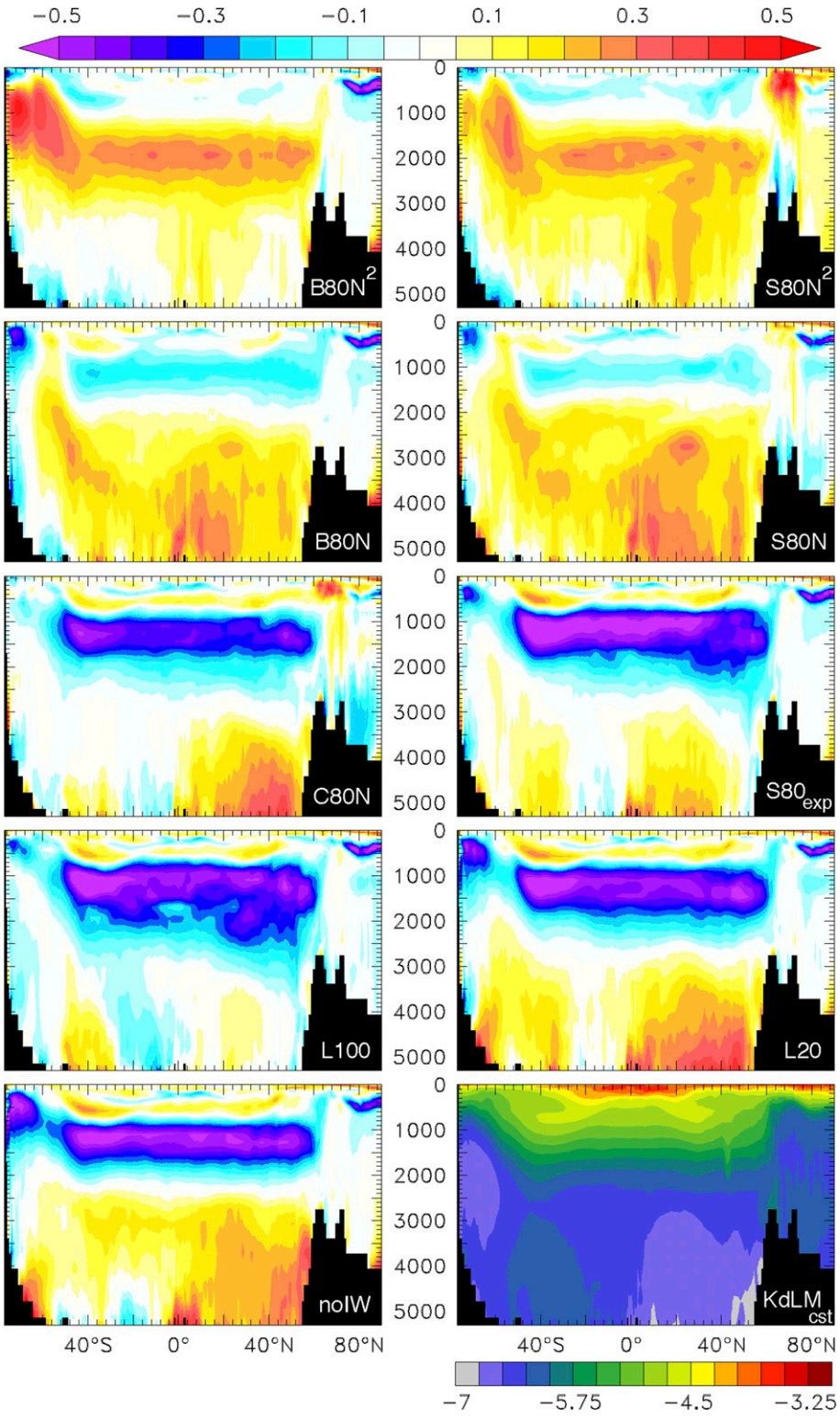


FIG. 7. Global zonal-mean stratification ($s^{-2}$) shown as a difference in $\log_{10}(\overline{N^2}^x)$ from the KdLMcst simulation. The color bar is shown across the top. Below the bottom-right panel, the corresponding color bar shows the logarithm of the global zonal-mean stratification ($s^{-2}$) for the KdLMcst simulation.

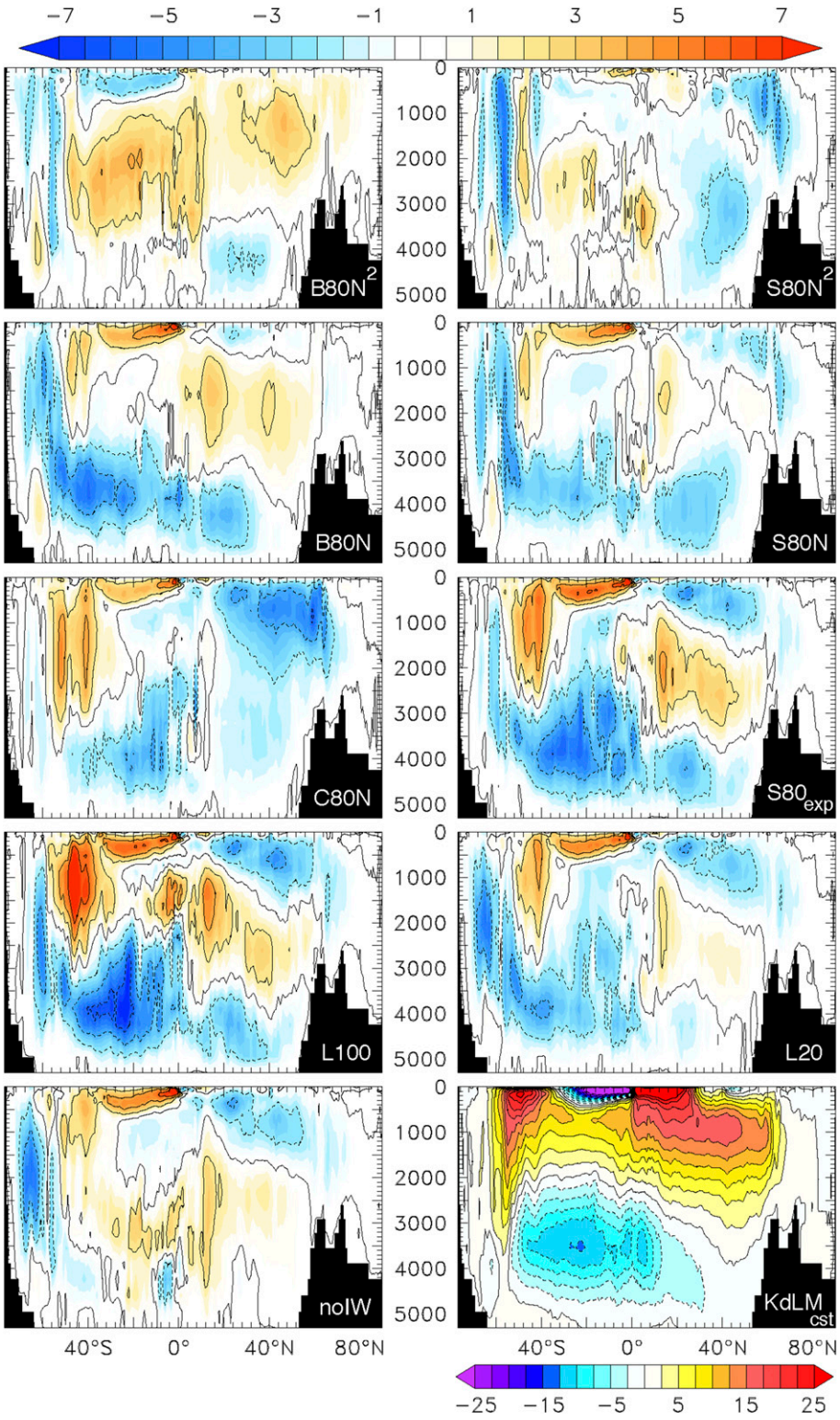


FIG. 8. The global MOC (Sv; 1 Sv $\equiv 10^6\ m^3\ s^{-1}$) shown as a difference in MOC from the KdLMcst simulation. The color bar is shown across the top. Below the bottom-right panel, the corresponding color bar shows the MOC (Sv) of the KdLMcst simulation.

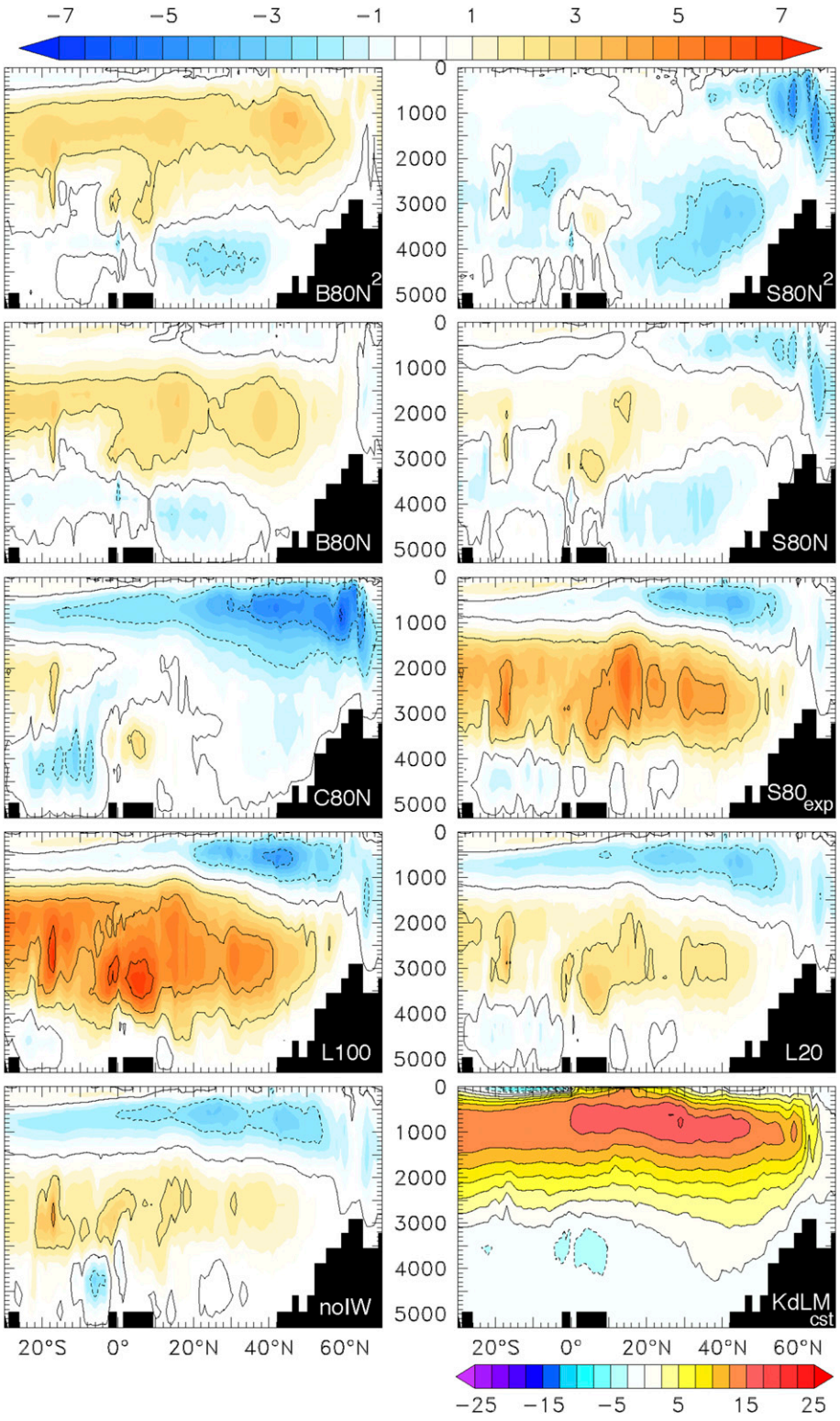


FIG. 9. The AMOC (Sv) shown as a difference in AMOC from the KdLMcst simulation. The color bar is shown across the top. Below the bottom-right panel, the corresponding color bar shows the AMOC (Sv) of the KdLMcst simulation.

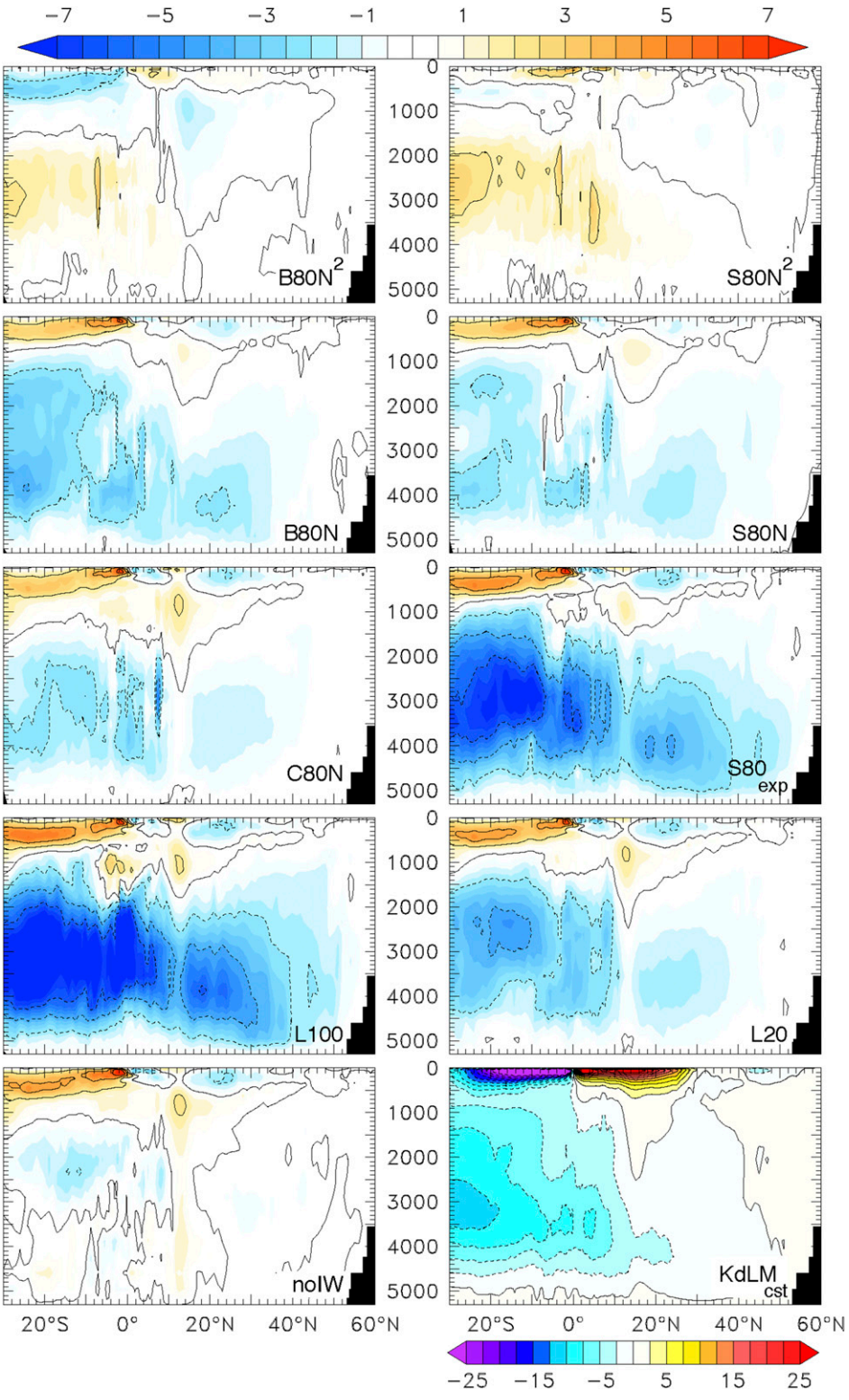


FIG. 10. The Indo-Pacific meridional overturning circulation (IPMOC; Sv) shown as a difference in IPMOC from the KdLMcst simulation. The color bar is shown across the top. Below the bottom-right panel, the corresponding color bar shows the IPMOC (Sv) of the KdLMcst simulation.

weaker Pacific subtropical overturning compared to KdLMcst, which has the strongest diffusivity in the upper thermocline apart from B80N$^2$ and S80N$^2$ (Fig. 10). In the Atlantic, the behavior is more complicated: while the Atlantic meridional overturning circulation (AMOC) is reduced in C80N and slightly reduced in S80N and S80N$^2$ compared to KdLMcst, it is strengthened and deepened in L100 and S80exp, and to a lesser extent in B80N and B80N$^2$ (Fig. 9). The fact that the AMOC is strengthened in B80N$^2$, although less deep than KdLMcst, suggests a sensitivity to the increase in diffusivity in shallower regions and reduction in deeper regions of the ocean basins in B80N$^2$ compared to KdLMcst. Finally, KdLMcst has a weak deep southern cell, as does C80N; reducing the mixing on the coastal shelves (S80exp, L100, and to a lesser extent L20, B80N, and S80N) leads to a stronger and denser southern cell (Figs. 8 and 10).

The ocean ventilation in climate models can be diagnosed from the ideal age tracer (Thiele and Sarmiento 1990). This tracer is set to zero in the bulk mixed layer and ages at a rate of 1 yr yr$^{-1}$ thereafter. In the deep ocean, the ideal age is small (young) in regions containing water recently modified by deep convection and large (old) in quiescent regions such as the Pacific subtropical gyres. In the simulations presented in this study, ideal ages are a function of the duration of the simulations, since these are shorter than the time scale of ventilation of the oldest water in the ocean (of roughly 1500 yr; e.g., England 1995). Nonetheless, the ideal age tracer, shown at the ocean bottom in Fig. 11, allows us to trace the movement of water of convective origin from its source in polar regions. When the deep mixing is small, young water resulting from deep convection extends through much of the deep Pacific (e.g., noIW and L20). For larger values of deep mixing, the Pacific bottom waters become older, as older deep waters are mixed into the bottom waters along its path (L100 and S80exp). C80N has weak deep mixing, but the dense water is diluted near the source on the shelves, resulting in a weaker southern overturning and hence older bottom waters in the Pacific. Similarly, KdLMcst has diluted bottom waters even in the Pacific sector of the Southern Ocean. In B80N$^2$ and S80N$^2$ there is much less deep convection in the Southern Ocean because of increased stratification. Young waters only reach part of the Southern Ocean seafloor (mostly in the Atlantic sector) and bottom waters are much older in the Indo-Pacific region than in other simulations.

Deep mixing has a more complicated influence on the age of Atlantic bottom waters, in part because of the two sources of young water. Away from the subpolar North Atlantic, B80N$^2$ and S80N$^2$ also have older bottom water in the Atlantic Ocean compared to other simulations. Regarding other simulations, the only significant difference in the North Atlantic between simulations is seen in S80N, which has a weaker North Atlantic overturning, and older bottom waters in the northwestern Atlantic. The North Atlantic Deep Water (NADW) appears to be most sensitive to the presence of enhanced mixing above the continental slopes, which is perhaps due to its source in the Nordic overflows, and in S80N lighter dense waters from the northern source may overlie older dense waters of Antarctic origin. The eastern Atlantic age varies with the density of the southern overturning cell: KdLMcst and C80N, with more dilute AABW, have older waters in the eastern Atlantic; L20 and noIW, with cold dense AABW, have the youngest eastern Atlantic waters.

Changes in the meridional overturning circulation (MOC) and temperature combine and lead to changes in the ocean meridional heat transport (MHT), which is key for the ocean influence on the atmosphere and the climate. The global MHT and its partition per oceanic basin are shown in Fig. 12. Only B80N$^2$ has a stronger global, Atlantic, Indo-Pacific and Southern Ocean MHT than KdLMcst, which could primarily be related to the warmer ocean temperature in B80N$^2$, especially in the upper ocean and thermocline (Figs. 6 and 8). In the Atlantic, the MHT is positive (northward), and all simulations other than B80N$^2$ exhibit negative anomalies of MHT relative to KdLMcst. This could be related to the deeper NADW cell in all simulations. The weakening in the Atlantic MHT compared to KdLMcst is stronger in C80N, S80N$^2$, L20, and noIW, as the upper part of the NADW overturning cell is weakened in these simulations. In the Indo-Pacific region, MHT anomalies reach 10%–15% of KdLMcst (150 TW) in the Southern Hemisphere. These negative anomalies are related to the weakening of the subtropical cell overturning circulation and the cooler upper and thermocline waters. By contrast, B80N$^2$ has slightly strengthened subtropical overturning cells and warmer upper and thermocline waters, resulting in a stronger MHT in the southern Indo-Pacific region.

### *d. Impact of remote diffusivity on ocean surface properties*

While mixing in the ocean interior is expected to have a direct influence on the deep circulation and stratification, surface properties can also be affected. The temperature differences at the sea surface are influenced by the local mixing in the thermocline and the overturning circulation, as well as the feedback on the atmospheric circulation. The spatial variation of sea surface temperature, shown as a difference from the KdLMcst simulation, is illustrated in Fig. 13.

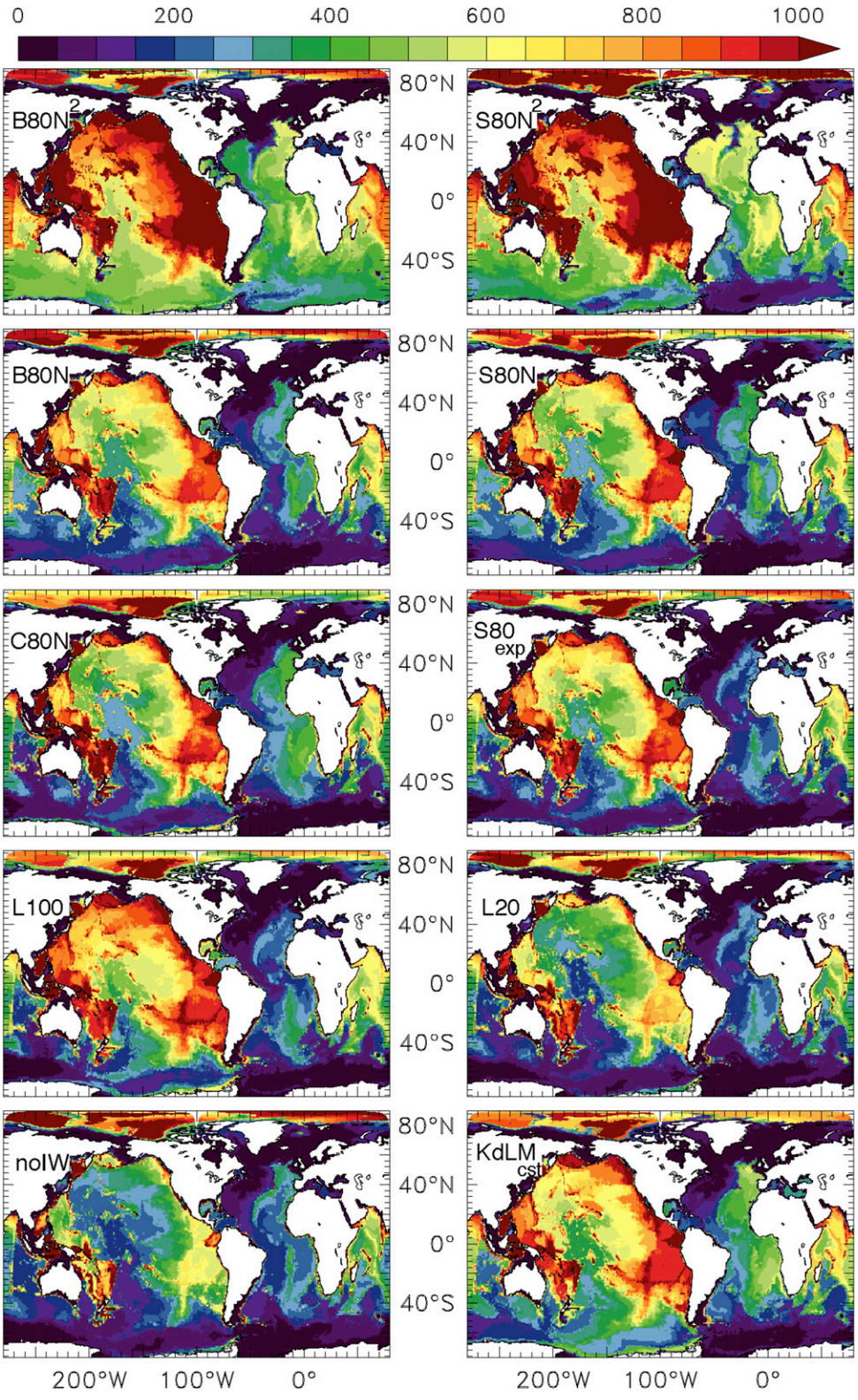


FIG. 11. Ideal age (yr) at the ocean bottom for all simulations.

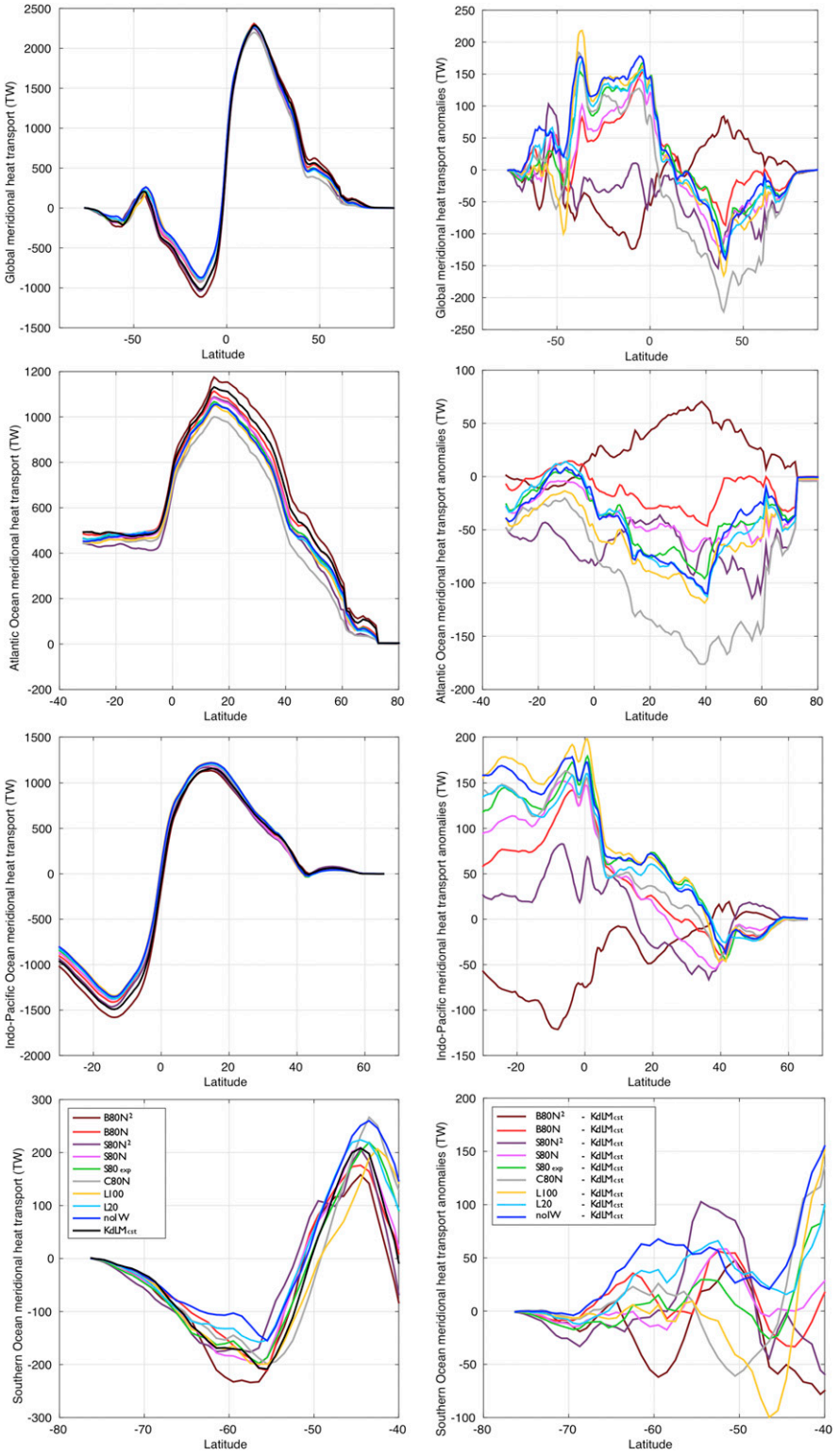


FIG. 12. (left) MHT (TW) and (right) MHT anomalies from the KdLMcst simulation (TW) for (top) the global ocean, (middle top) the Atlantic Ocean, (middle bottom) the Indo-Pacific region, and (bottom) the Southern Ocean. The color codes given in the bottom panels are the same as in Fig. 2 for the right panels and Fig. 5 for the left panels.

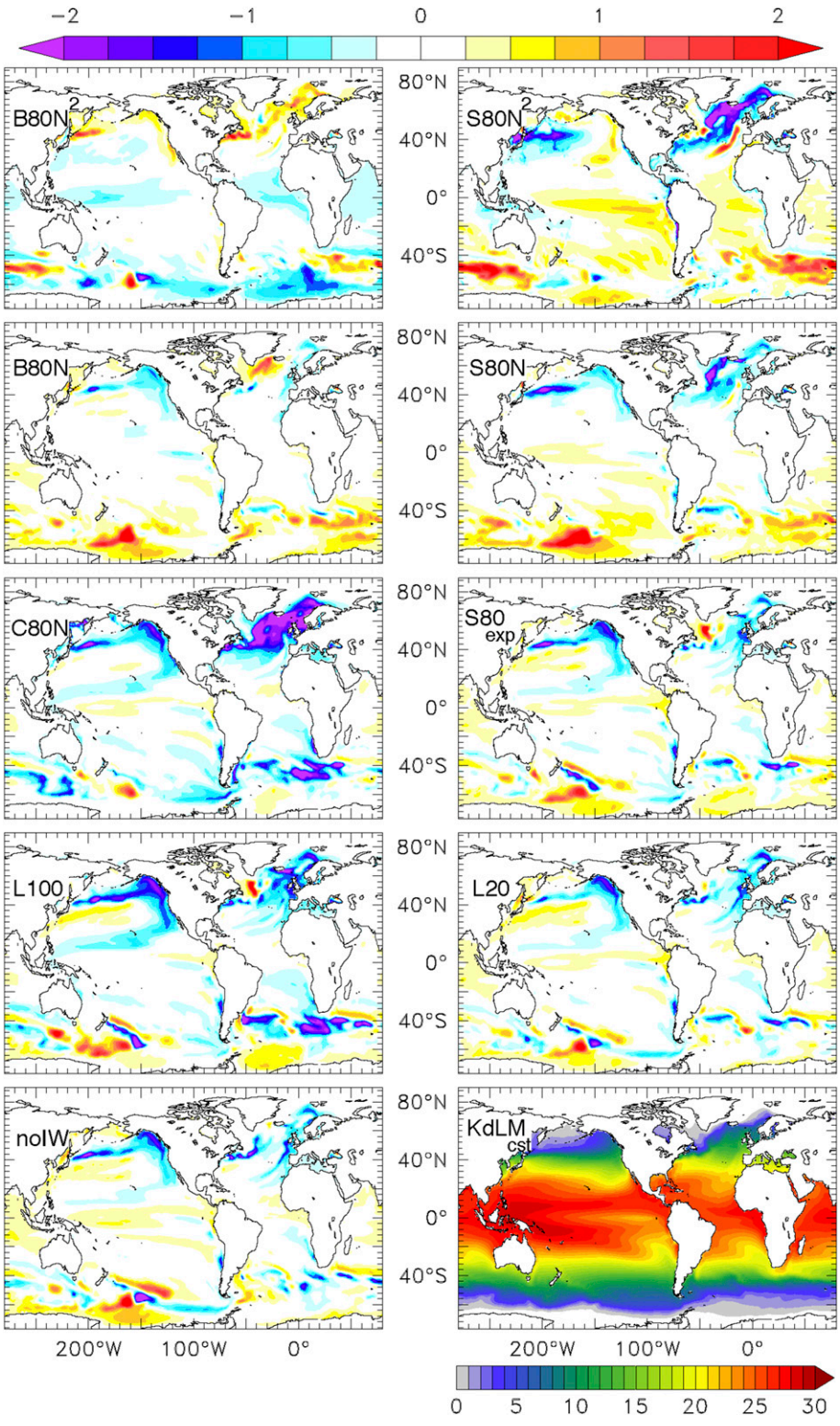


FIG. 13. SST (°C) shown as an SST difference from the KdLMcst simulation. The color bar is shown across the top. Below the bottom-right panel, the corresponding color bar shows the SST (°C) of the KdLMcst simulation.

Compared to KdLMcst, simulations with a weaker thermocline diffusivity (cases noIW, L20, and S80exp) have a slightly warmer equatorial eastern Pacific upwelling region (i.e., just south of Panama), consistent with the reduction in the Pacific equatorial upwelling. Large differences seen in the subpolar North Atlantic may reflect different North Atlantic overturning; for example, C80N has a much colder subpolar North Atlantic, coinciding with a weak AMOC in the northern Atlantic, as do S80N$^2$ and S80N to a lesser extent. Both B80N$^2$ and B80N show some North Atlantic warming, and both have a stronger AMOC. These differences persist over several hundred years and, therefore, do not result from AMOC variability at shorter time scales. Compared to other simulations, S80N$^2$, S80N, and B80N have a warmer Southern Ocean, perhaps because upper deep water, warmed by increased diffusivity at depth (Fig. 6), outcrops in this region. Some anomalies seen in the Southern Ocean (e.g., in the region of 160°W) are transient and do not persist over multiple centuries; we currently have no explanation for these anomalies relative to KdLMcst.

Diapycnal mixing directly impacts the ocean heat uptake and the distribution of heat in the ocean (e.g., Hallberg et al. 2013; Kuhlbrodt and Gregory 2012). The impact of low-mode energy dissipation on the thermosteric component of sea level is shown in Fig. 14, as a difference from the KdLMcst simulation. Since the thermal expansion coefficient is larger for warmer water, increases in thermosteric sea level are an indicator of increased heat uptake in warmer regions of the ocean. Both B80N$^2$ and S80N$^2$ have larger diffusivities than KdLMcst in the thermocline, leading to the warmest and thickest thermoclines, while all other simulations have lower diffusivities in the thermocline. Therefore, B80N$^2$ and S80N$^2$ show higher thermosteric sea level than KdLMcst while all other simulations show lower thermosteric sea level. The smallest negative differences are seen for B80N and S80N, which have diffusivities in the thermocline that are more similar to that of KdLMcst. The largest negative differences are seen for L20 and noIW, correlating with the thermocline temperatures and thicknesses. C80N shows lower sea level in the equatorial Pacific but similar sea level in the equatorial Atlantic compared to KdLMcst, while L100 shows lower sea level in the Atlantic, perhaps reflecting the different distributions of coastal shelves versus deep topography in the two basins. These results suggest that using a more energetically constrained parameterization of low-mode internal-tide dissipation significantly impacts the simulated ocean heat uptake in the upper ocean and thermosteric sea level (Kuhlbrodt and Gregory 2012).

### e. *Summary of the physical impacts of remote diffusivity on the ocean state*

To summarize, weak mixing in the ocean interior (e.g., L20) leads to cooler interior temperatures overall and weak deep overturning as the abyss slowly fills with bottom water of Antarctic origin. Strong deep mixing (e.g., L100) leads to abyssal warming and enhancement of both the northern and southern deep overturning cells. Strong mixing on shelves (e.g., C80N and KdLMcst) disproportionately influences the AABW, warming and weakening the southern overturning cell.

Weak diffusivity in the thermocline (L20, L100, S80exp, C80N, and to a lesser extent B80N and S80N) leads to a sharper thermocline, and weaker subtropical overturning in the Pacific. Strong diffusivities in the thermocline (B80N$^2$ and S80N$^2$) lead to a broader thermocline, warmer ocean, higher steric sea level, and less deep convection in the Southern Ocean. Little mixing on shelves and moderate mixing at depth (B80N and S80N) leads to cooler AABW and a denser, stronger southern overturning cell and greater deep stratification. B80N and S80N also have enhanced diffusivities in the upper deep water (e.g., 2000-m depth) that tends to warm the North Atlantic Deep Water leading to a warming of sea surface temperature in the Southern Ocean where this water outcrops. The similarity between the B80N and S80N results, despite the somewhat greater diffusivity at depth in B80N, indicates the importance of the stratification dependence of the dissipation profile. Similarly, S80exp produces results that more closely resemble L100, which has a similar vertical distribution of dissipation, as opposed to S80N, which has the same horizontal distribution of dissipation. The vertical profile of diffusivity is therefore more important for global quantities than the horizontal distribution, provided that distribution is in the open ocean (i.e., not on coastal shelves).

The differences between B80N$^2$ and S80N$^2$ on one hand and KdLMcst on the other are important. All have remote diffusivities that are locally independent of depth; however, whereas KdLMcst has a constant diffusivity everywhere, in B80N$^2$ and S80N$^2$ the diffusivity is inversely proportional to the total depth, so that shallower regions have greater diffusivities, and deeper regions lower diffusivities. This is a consequence of the assumption of uniform far-field energy distribution per unit area within the basin or slope region, an assumption that may need reevaluation.

Mixing on coastal shelves only impacts the large-scale circulation and water mass properties if it modifies water masses originating on shelves (e.g., AABW). However, the North Atlantic overturning, and consequent sea

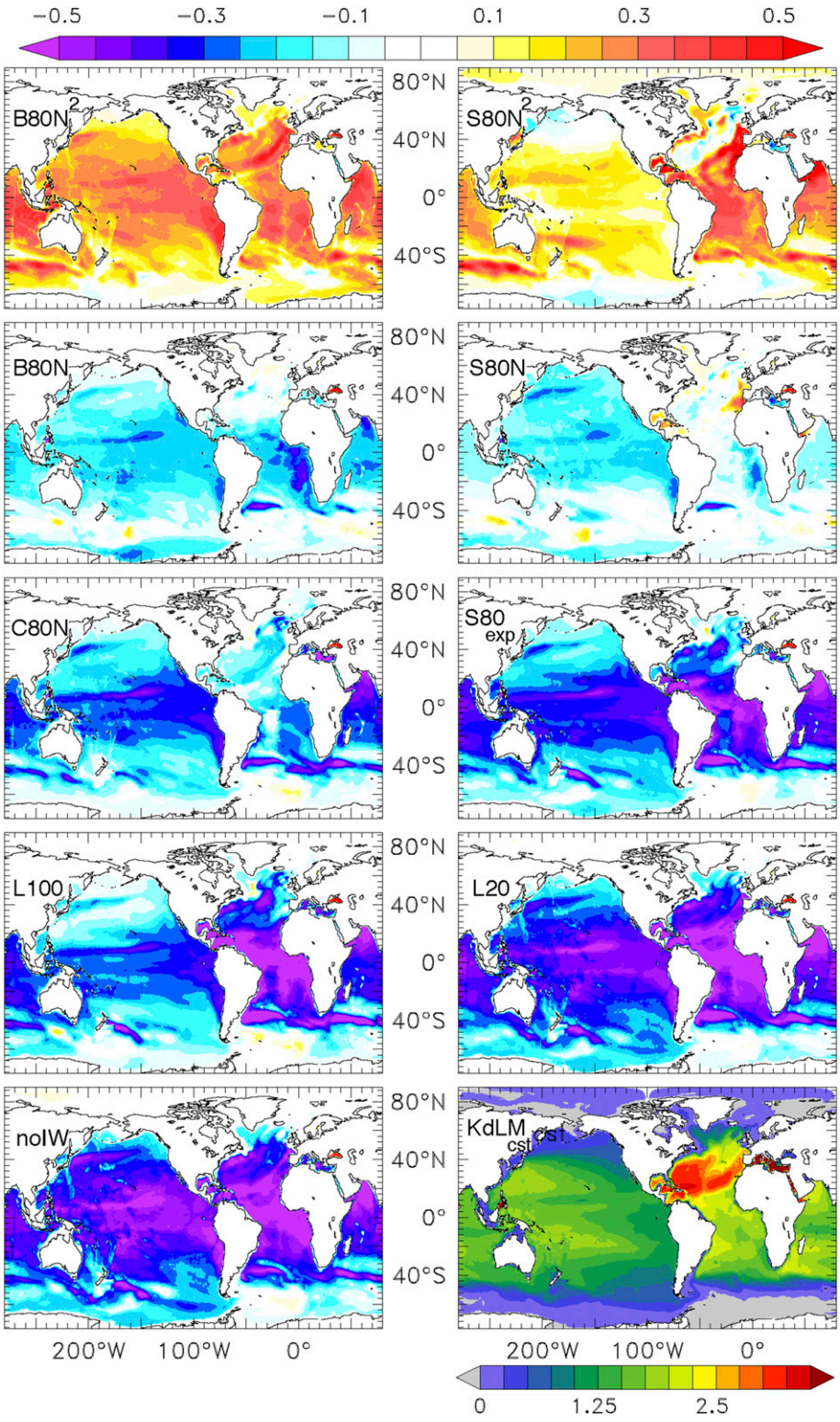


FIG. 14. Thermosteric sea level (TSSL) referenced at the ocean bottom (m) shown as a difference in TSSL from the KdLMcst simulation. The color bar is shown across the top. Below the bottom-right panel, the corresponding color bar shows the TSSL (m) of the KdLMcst simulation.

surface temperatures do show significant differences between S80N and B80N, and between $S80N^2$ and $B80N^2$, indicating one area where circulation is sensitive to the horizontal distribution of mixing, perhaps because localized mixing can significantly impact the downwelling branch of the AMOC (Scott and Marotzke 2002).

## 4. Discussion

The impacts on Pacific overturning circulation are found to be of smaller amplitude than those reported by Oka and Niwa (2013), who used a remote dissipation profile that is constant with depth and added to the background diffusion, in contrast to the different remote dissipation profiles that replace the background diffusion. The horizontal distribution is also different: Oka and Niwa (2013) use the vertically integrated tidal dissipation from a 3D tidal model run for 60 days to specify the horizontal distribution of the remote dissipation, while we explore the implications of different idealized horizontal distributions of dissipation.

Our simulations are in agreement with the diagnostic study of de Lavergne et al. (2015a), who examine the implications of different horizontal and vertical distributions of remote internal-tide mixing for the lightening of Antarctic Bottom Water. We find a similar sensitivity to the vertical profile of the remote dissipation. In particular, de Lavergne et al. (2015a) show that a dissipation profile that is proportional to the buoyancy frequency is consistent with the required transformation of AABW necessary to balance the observed AABW production. As in de Lavergne et al. (2015a), we find smaller sensitivity to the horizontal distribution. While de Lavergne et al. (2015a) highlight the importance of mixing in the Southern Ocean, our results also show that the horizontal distribution of mixing in regions near the downwelling limbs of the overturning cells is particularly important (e.g., the Antarctic shelves and the subpolar North Atlantic). Our prognostic simulations extend the work of de Lavergne et al. (2015a) to examine the impact of the remote mixing on the ocean stratification, circulation, and surface properties in a self-consistent manner.

Our study and those of de Lavergne et al. (2015a) and Oka and Niwa (2013) all point to the importance of the remote component of internal-tide dissipation, as well as the inadequacy of a uniform diffusion to account for this process. However, our idealized sensitivity studies are far from providing a complete parameterization of remote dissipation. First, we assume that a constant fraction of internal-tide energy is dissipated locally, either 20% or 100%, whereas observations (Falahat et al. 2014), numerical simulations (Nikurashin and Legg 2011; Klymak et al. 2010), and analytical studies (Lefauve et al. 2015) suggest that the local fraction of dissipation varies as a function of the type of topography, the tidal amplitudes, and the Coriolis parameter and depends on several different processes (e.g., internal hydraulic jumps, wave–wave interactions, and wave saturation). A more realistic local and remote dissipation model requires the development of a physically based parameterization of the temporally and spatially varying fraction of local dissipation $q_L$. Second, we have assumed that the remote dissipation is uniformly distributed, by area, over either the basins, slopes, or shelves. In the real ocean, the horizontal distribution of dissipation will be more spatially variable, depending on the propagation of the low-mode waves away from their generation sites, and will include a combination of basins, slopes, and shelves. A wave propagation model is required to correctly represent this aspect of the remote dissipation. Eden and Olbers (2014) describe one possibility, in which the low-mode energy propagates radially out from the generation sites; in reality, the internal-wave energy propagates along beams (Alford and Zhao 2007). As low modes propagate, energy may be lost through scattering from bottom topography (Bühler and Holmes-Cerfon 2011), through wave–wave interaction (MacKinnon and Winters 2005), and through interaction with mesoscale eddies and mean currents (Polzin 2008). Models for low-mode attenuation and dissipation due to these processes are required. Finally, low-mode energy encountering a continental slope may undergo one of several processes: reflection back into the deep ocean, in which case there is little dissipation (Klymak et al. 2013); critical reflection, when dissipation is localized at the slope (Ivey and Nokes 1989; Martini et al. 2013); shoaling at subcritical slopes, where dissipation is then spread through the water column in proportion to the stratification (Legg 2014); and finally transmission up onto the shelf of any energy that is not dissipated or reflected. At any particular continental slope, some fraction may be reflected, some dissipated, and some transmitted (Johnston et al. 2015). Kelly et al. (2013) attempts to determine the net energy reflected and transmitted onto the shelf for all locations around the global continental slope, a necessary component for any complete parameterization. We anticipate that the full realistic distribution of low-mode mixing will contain some combination of mixing in basins, over rough topography, over the slopes in the full water column, over critical slopes, and on the continental shelves, combining aspects of several of our idealized scenarios. The extent to which mixing occurs near the downwelling branch of the overturning circulation (i.e., on Antarctic shelves or near the descending boundary currents of the North Atlantic) will

be particularly important to determine, since our study has shown that the large-scale circulation is sensitive to details of mixing in those locations.

## 5. Conclusions

We have presented an idealized study of the impact of the remote dissipation of low-mode internal waves on the large-scale circulation. The remote dissipation was energetically constrained, and specified to occur either at the generation sites, in deep basins, on continental slopes. or on continental shelves. The simulations presented here exhibit significant differences in the ocean circulation and water-mass structure between simulations with the same amount of turbulent dissipation but different lateral and vertical distributions of that mixing. In contrast to most earlier studies of the impact of internal tides, the remote mixing component is represented through a vertical profile of dissipation that either scales with the squared buoyancy frequency or the buoyancy frequency or is bottom intensified, which can be justified for different types of wave breaking (wave–wave interactions and shoaling or critical reflection and scattering from rough topography). The vertical profile of dissipation is shown to influence the circulation and stratification more strongly than the horizontal distribution, provided that horizontal distribution is within the open ocean: dissipation on coastal shelves by contrast has little impact on the large-scale circulation except in regions of dense water formation, such as the Antarctic shelves. Compared to the commonly used constant background diffusivity, a remote dissipation profile that is proportional to buoyancy frequency leads to lower diffusivities in the upper ocean, resulting in a less diffuse thermocline and less heat uptake in the upper ocean, with lower associated thermosteric sea level. Diffusivities at depth are higher than for a constant-diffusivity representation, resulting in more vigorous deep overturning. On the contrary, a remote dissipation profile that is proportional to the squared buoyancy frequency (so that diffusivity is locally depth independent) combined with a uniform distribution of energy by area within the prescribed region leads to higher diffusivities in shallow regions and lower diffusivities in deeper regions. On average then, upper-ocean diffusivities are higher, resulting in a more diffuse thermocline, and more heat uptake in the upper ocean, with higher associated thermosteric sea level and stronger meridional heat transport. For horizontal distributions with less dissipation near the origins of deep water in the North Atlantic or Antarctic, denser bottom water results. Changes in the overturning lead in turn to changes in the ideal age tracer and in surface temperature. These in turn are likely to have implications for the ability of deep waters to uptake and store $CO_2$, which will be a topic of future investigation. The results presented here emphasize the importance of developing energetically consistent parameterizations of internal-tide mixing with spatial distributions that accurately reflect the physical processes that occur in the ocean.

*Acknowledgments.* The authors thank Stephen Griffies and Rong Zhang for reviewing early versions of this manuscript, and three anonymous reviewers for helpful comments leading to improvements in the manuscript. This work is the internal-wave driven mixing component of the Climate Process Team funded by the National Science Fundation (Grant OCE-0968721) and the National Oceanic and Atmospheric Administration of the U.S. Department of Commerce (Award NA08OAR4320752). The statements, findings, conclusions, and recommendations are those of the authors and do not necessarily reflect the views of the National Oceanic and Atmospheric Administration or the U.S. Department of Commerce.

## REFERENCES

Adcroft, A., J. R. Scott, and J. Marotzke, 2001: Impact of geothermal heating on the global ocean circulation. *Geophys. Res. Lett.*, **28**, 1735–1738, doi:10.1029/2000GL012182.

Alford, M. H., 2001: Internal swell generation: The spatial distribution of energy flux from the wind to mixed layer near-inertial motions. *J. Phys. Oceanogr.*, **31**, 2359–2368, doi:10.1175/1520-0485(2001)031<2359:ISGTSD>2.0.CO;2.

——, 2003: Energy available for ocean mixing redistributed through long-range propagation of internal waves. *Nature*, **423**, 159–163, doi:10.1038/nature01628.

——, and Z. Zhao, 2007: Global patterns of low-mode internal-wave propagation. Part I: Energy and energy flux. *J. Phys. Oceanogr.*, **37**, 1829–1848, doi:10.1175/JPO3085.1.

Althaus, A., E. Kunze, and T. Sanford, 2003: Internal tide radiation from Mendocino Escarpment. *J. Phys. Oceanogr.*, **33**, 1510–1527, doi:10.1175/1520-0485(2003)033<1510:ITRFME>2.0.CO;2.

Arbic, B. K., A. J. Wallcraft, and E. J. Metzger, 2010: Concurrent simulation of the eddying general circulation and tides in a global ocean model. *Ocean Modell.*, **32**, 175–187, doi:10.1016/j.ocemod.2010.01.007.

Aucan, J., M. A. Merrifield, S. D. Luther, and P. Flament, 2006: Tidal mixing events on the deep flanks of Kaena Ridge, Hawaii. *J. Phys. Oceanogr.*, **36**, 1202–1219, doi:10.1175/JPO2888.1.

Bell, T. H., 1975: Topographically generated internal waves in the open ocean. *J. Geophys. Res.*, **80**, 320–327, doi:10.1029/JC080i003p00320.

Bessières, L., G. Madec, and F. Lyard, 2008: Global tidal residual mean circulation: Does it affect a climate OGCM? *Geophys. Res. Lett.*, **35**, L03609, doi:10.1029/2007GL032644.

Bouffard, D., and L. Boegman, 2013: A diapycnal diffusivity model for stratified environmental flows. *Dyn. Atmos. Oceans*, **61–62**, 14–34, doi:10.1016/j.dynatmoce.2013.02.002.

Bryan, F. O., 1987: Parameter sensitivity of primitive equation ocean general circulation models. *J. Phys. Oceanogr.*, **17**, 970–985, doi:10.1175/1520-0485(1987)017<0970:PSOPEO>2.0.CO;2.

Bühler, O., and M. Holmes-Cerfon, 2011: Decay of an internal tide due to random topography in the ocean. *J. Fluid Mech.*, **678**, 271–293, doi:10.1017/jfm.2011.115.

Carter, G. S., and M. Gregg, 2002: Intense, variable mixing near the head of Monterey Submarine Canyon. *J. Phys. Oceanogr.*, **32**, 3145–3165, doi:10.1175/1520-0485(2002)032<3145:IVMNTH>2.0.CO;2.

——, M. C. Gregg, and M. A. Merrifield, 2006: Flow and mixing around a small seamount on Kaena Ridge, Hawaii. *J. Phys. Oceanogr.*, **36**, 1036–1052, doi:10.1175/JPO2924.1.

Cummins, P. F., J. Y. Cherniawsky, and M. G. G. Foreman, 2001: North Pacific internal tides from the Aleutian Ridge: Altimeter observations and modeling. *J. Mar. Res.*, **59**, 167–191, doi:10.1357/002224001762882628.

Dalan, F., P. H. Stone, and A. P. Sokolov, 2005: Sensitivity of the ocean's climate to diapycnal diffusivity in an EMIC. Part II: Global warming scenario. *J. Climate*, **18**, 2482–2496, doi:10.1175/JCLI3412.1.

D'Asaro, E., 1985: The energy flux from the wind to near-inertial motions in the mixed layer. *J. Phys. Oceanogr.*, **15**, 943–959, doi:10.1175/1520-0485(1985)015<0943:UOTSIC>2.0.CO;2.

Decloedt, T., and D. Luther, 2010: On a simple empirical parameterization of topography-catalyzed diapycnal mixing in the abyssal ocean. *J. Phys. Oceanogr.*, **40**, 487–508, doi:10.1175/2009JPO4275.1.

de Lavergne, C., G. Madec, J. Sommer, A. J. Nurser, and A. C. Naveira Garabato, 2015a: On the consumption of Antarctic bottom water in the abyssal ocean. *J. Phys. Oceanogr.*, **46**, 635–661, doi:10.1175/JPO-D-14-0201.1.

——, ——, ——, ——, and ——, 2015b: The impact of a variable mixing efficiency on the abyssal overturning. *J. Phys. Oceanogr.*, **46**, 663–681, doi:10.1175/JPO-D-14-0259.1.

Dunne, J. P., and Coauthors, 2012: GFDL's ESM2 global coupled climate–carbon Earth system models. Part I: Physical formulation and baseline simulation characteristics. *J. Climate*, **25**, 6646–6665, doi:10.1175/JCLI-D-11-00560.1.

Dushaw, B., 2002: Mapping low-mode internal tides near Hawaii using TOPEX/POSEIDON altimeter data. *Geophys. Res. Lett.*, **29**, 1250, doi:10.1029/2001GL013944.

Eden, C., and D. Olbers, 2014: An energy compartment model for propagation, nonlinear interaction, and dissipation of internal gravity waves. *J. Phys. Oceanogr.*, **44**, 2093–2106, doi:10.1175/JPO-D-13-0224.1.

Egbert, G. D., and R. D. Ray, 2000: Significant dissipation of tidal energy in the deep ocean inferred from satellite altimeter data. *Nature*, **405**, 775–778, doi:10.1038/35015531.

——, and S. Y. Erofeeva, 2002: Efficient inverse modeling of barotropic ocean tides. *J. Atmos. Oceanic Technol.*, **19**, 183–204, doi:10.1175/1520-0426(2002)019<0183:EIMOBO>2.0.CO;2.

England, M. H., 1995: The age of water and ventilation timescales in a global ocean model. *J. Phys. Oceanogr.*, **25**, 2756–2777, doi:10.1175/1520-0485(1995)025<2756:TAOWAV>2.0.CO;2.

Falahat, S., J. Nycander, F. Roquet, A. Thurnherr, and T. Hibiya, 2014: Comparison of calculated energy flux of internal tides with microstructure measurements. *Tellus*, **66A**, 23240, doi:10.3402/tellusa.v66.23240.

Ferron, B., H. Mercier, K. Speer, A. Gargett, and K. Polzin, 1998: Mixing in the Romanche Fracture Zone. *J. Phys. Oceanogr.*, **28**, 1929–1945, doi:10.1175/1520-0485(1998)028<1929:MITRFZ>2.0.CO;2.

Gargett, A. E., 1984: Vertical eddy diffusivity in the ocean interior. *J. Mar. Res.*, **42**, 359–393, doi:10.1357/002224084788502756.

——, and G. Holloway, 1984: Dissipation and diffusion by internal wave breaking. *J. Mar. Res.*, **42**, 15–27, doi:10.1357/002224084788506158.

Garrett, C., and E. Kunze, 2007: Internal tide generation in the deep ocean. *Annu. Rev. Fluid Mech.*, **39**, 57–87, doi:10.1146/annurev.fluid.39.050905.110227.

Gill, A. E., 1982: *Atmosphere–Ocean Dynamics*. International Geophysics Series, Vol. 30, Academic Press, 662 pp.

Gnanadesikan, A., B. L. Samuels, and R. D. Slater, 2003: Sensitivity of water mass transformation and heat transport to subgridscale mixing in coarse-resolution ocean models. *Geophys. Res. Lett.*, **30**, 1967, doi:10.1029/2003GL018036.

——, J. P. Dunne, R. M. Key, K. Matsumoto, J. L. Sarmiento, R. D. Slater, and P. S. Swathi, 2004: Oceanic ventilation and biogeochemical cycling: Understanding the physical mechanisms that produce realistic distributions of tracers and productivity. *Global Biogeochem. Cycles*, **18**, GB4010, doi:10.1029/2003GB002097.

Gregg, M. C., 1989: Scaling turbulent dissipation in the thermocline. *J. Geophys. Res.*, **94**, 9686–9698, doi:10.1029/JC094iC07p09686.

——, T. B. Sanford, and D. P. Winkel, 2003: Reduced mixing from the breaking of internal waves in equatorial waters. *Nature*, **422**, 513–515, doi:10.1038/nature01507.

——, R. A. Hall, G. Carter, M. H. Alford, R.-C. Lien, D. P. Winkel, and D. J. Wain, 2011: Flow and mixing in Ascension, a steep narrow canyon. *J. Geophys. Res.*, **116**, C07016, doi:10.1029/2010JC006610.

Griffies, S. M., R. C. Pacanowski, and R. W. Hallberg, 2000: Spurious diapycnal mixing associated with advection in a *z*-coordinate ocean model. *Mon. Wea. Rev.*, **128**, 538–564, doi:10.1175/1520-0493(2000)128<0538:SDMAWA>2.0.CO;2.

Hallberg, R., 2003: The ability of large-scale ocean models to accept parameterizations of boundary mixing, and a description of a refined bulk mixed-layer model. *Internal Gravity Waves and Small-Scale Turbulence: Proc. 'Aha Huliko'a Hawaiian Winter Workshop*, Honolulu, HI, University of Hawai'i at Mānoa, 187–203. [Available online at http://www.soest.hawaii.edu/PubServices/2003pdfs/Hallberg.pdf.]

——, and A. Adcroft, 2009: Reconciling estimates of the free surface height in Lagrangian vertical coordinate ocean models with mode-split time stepping. *Ocean Modell.*, **29**, 15–26, doi:10.1016/j.ocemod.2009.02.008.

——, ——, J. P. Dunne, J. P. Krasting, and R. J. Stouffer, 2013: Sensitivity of twenty-first-century global-mean steric sea level rise to ocean model formulation. *J. Climate*, **26**, 2947–2956, doi:10.1175/JCLI-D-12-00506.1.

Harrison, M. J., and R. W. Hallberg, 2008: Pacific subtropical cell response to reduced equatorial dissipation. *J. Phys. Oceanogr.*, **38**, 1894–1912, doi:10.1175/2008JPO3708.1.

Henyey, F. S., J. Wright, and S. M. Flatté, 1986: Energy and action flow through the internal wave field: An eikonal approach. *J. Geophys. Res.*, **91**, 8487–8496, doi:10.1029/JC091iC07p08487.

Huang, R. X., 1999: Mixing and energetics of the oceanic thermohaline circulation. *J. Phys. Oceanogr.*, **29**, 727–746, doi:10.1175/1520-0485(1999)029<0727:MAEOTO>2.0.CO;2.

Ilicak, M., A. Adcroft, S. M. Griffies, and R. Hallberg, 2012: Spurious dianeutral mixing and the role of momentum closure. *Ocean Modell.*, **45–46**, 37–58, doi:10.1016/j.ocemod.2011.10.003.

Ivey, G., and R. Nokes, 1989: Vertical mixing due to the breaking of critical internal waves on sloping boundaries. *J. Fluid Mech.*, **204**, 479–500, doi:10.1017/S0022112089001849.

Jachec, S. M., O. B. Fringer, M. G. Gerritsen, and R. L. Street, 2006: Numerical simulation of internal tides and the

resulting energetics within Monterey Bay and the surrounding area. *Geophys. Res. Lett.*, **33**, L12605, doi:10.1029/2006GL026314.

Jackson, L., R. Hallberg, and S. Legg, 2008: A parameterization of shear-driven turbulence for ocean climate models. *J. Phys. Oceanogr.*, **38**, 1033–1053, doi:10.1175/2007JPO3779.1.

Jayne, S. R., 2009: The impact of abyssal mixing parameterizations in an ocean general circulation model. *J. Phys. Oceanogr.*, **39**, 1756–1775, doi:10.1175/2009JPO4085.1.

——, and L. C. St. Laurent, 2001: Parameterizing tidal dissipation over rough topography. *Geophys. Res. Lett.*, **28**, 811–814, doi:10.1029/2000GL012044.

Johnston, T. M. S., and M. A. Merrifield, 2003: Internal tide scattering at seamounts, ridges, and islands. *J. Geophys. Res.*, **108**, 3180, doi:10.1029/2002JC001528.

——, D. Rudnick, and S. Kelly, 2015: Standing internal tides in the Tasman Sea observed by gliders. *J. Phys. Oceanogr.*, **45**, 2715–2737, doi:10.1175/JPO-D-15-0038.1.

Kantha, L., and C. Tierney, 1997: Global baroclinic tides. *Prog. Oceanogr.*, **40**, 163–178, doi:10.1016/S0079-6611(97)00028-1.

Kelly, S., N. Jones, J. Nash, and A. Waterhouse, 2013: The geography of semidiurnal mode-1 internal-tide energy loss. *Geophys. Res. Lett.*, **40**, 4689–4693, doi:10.1002/grl.50872.

Klymak, J. M., and Coauthors, 2006: An estimate of tidal energy lost to turbulence at the Hawaiian ridge. *J. Phys. Oceanogr.*, **36**, 1148–1164, doi:10.1175/JPO2885.1.

——, R. Pinkel, and L. N. Rainville, 2008: Direct breaking of the internal tide near topography: Kaena Ridge, Hawaii. *J. Phys. Oceanogr.*, **38**, 380–399, doi:10.1175/2007JPO3728.1.

——, S. A. Legg, and R. Pinkel, 2010: A simple parameterization of turbulent tidal mixing near supercritical topography. *J. Phys. Oceanogr.*, **40**, 2059–2074, doi:10.1175/2010JPO4396.1.

——, M. H. Alford, R. Pinkel, R.-C. Lien, Y.-J. Yang, and T.-Y. Tang, 2011: The breaking and scattering of the internal tide on a continental slope. *J. Phys. Oceanogr.*, **41**, 926–945, doi:10.1175/2010JPO4500.1.

——, M. Buijsman, S. Legg, and R. Pinkel, 2013: Parameterizing surface and internal tide scattering and breaking on supercritical topography: The one- and two-ridge cases. *J. Phys. Oceanogr.*, **43**, 1380–1397, doi:10.1175/JPO-D-12-061.1.

Kuhlbrodt, T., and J. M. Gregory, 2012: Ocean heat uptake and its consequences for the magnitude of sea level rise and climate change. *Geophys. Res. Lett.*, **39**, L18608, doi:10.1029/2012GL052952.

Kunze, E., C. MacKay, E. E. McPhee-Shaw, K. Morrice, J. B. Girton, and S. R. Terker, 2012: Turbulent mixing and exchange with interior waters on sloping boundaries. *J. Phys. Oceanogr.*, **42**, 910–927, doi:10.1175/JPO-D-11-075.1.

Lee, C. M., E. Kunze, T. B. Sanford, J. D. Nash, M. A. Merrifield, and P. E. Holloway, 2006: Internal tides and turbulence along the 3000-m isobath of the Hawaiian Ridge. *J. Phys. Oceanogr.*, **36**, 1165–1183, doi:10.1175/JPO2886.1.

Lee, I.-H., R.-C. Lien, J. T. Liu, and W.-S. Chuang, 2009: Turbulence mixing and internal tides in Gaoping (Kaoping) Submarine Canyon. *J. Mar. Syst.*, **76**, 383–396, doi:10.1016/j.jmarsys.2007.08.005.

Lefauve, A., C. Muller, and A. Melet, 2015: A three-dimensional map of tidal dissipation over abyssal hills. *J. Geophys. Res. Oceans*, **120**, 4760–4777, doi:10.1002/2014JC010598.

Legg, S., 2014: Scattering of low-mode internal waves at finite isolated topography. *J. Phys. Oceanogr.*, **44**, 359–383, doi:10.1175/JPO-D-12-0241.1.

——, R. Hallberg, and J. Girton, 2006: Comparison of entrainment in overflows simulated by z-coordinate, isopycnal and nonhydrostatic models. *Ocean Modell.*, **11**, 69–97, doi:10.1016/j.ocemod.2004.11.006.

Lueck, R. G., and T. D. Mudge, 1997: Topographically induced mixing around a shallow seamount. *Science*, **276**, 1831–1833, doi:10.1126/science.276.5320.1831.

MacKinnon, J. A., and K. B. Winters, 2005: Subtropical catastrophe: Significant loss of low-mode tidal energy at 28.9°. *Geophys. Res. Lett.*, **32**, L15605, doi:10.1029/2005GL023376.

——, T. M. S. Johnston, and R. Pinkel, 2008: Strong transport and mixing of deep water through the Southwest Indian Ridge. *Nat. Geosci.*, **1**, 755–758, doi:10.1038/ngeo340.

Martini, K., M. H. Alford, E. Kunze, S. M. Kelly, and J. D. Nash, 2011: Observations of internal tides on the Oregon continental slope. *J. Phys. Oceanogr.*, **41**, 1772–1794, doi:10.1175/2011JPO4581.1.

——, ——, ——, ——, and ——, 2013: Internal bores and breaking internal tides on the Oregon continental slope. *J. Phys. Oceanogr.*, **43**, 120–139, doi:10.1175/JPO-D-12-030.1.

McComas, C. H., and P. Müller, 1981: The dynamic balance of internal waves. *J. Phys. Oceanogr.*, **11**, 970–986, doi:10.1175/1520-0485(1981)011<0970:TDBOIW>2.0.CO;2.

Melet, A., R. Hallberg, S. Legg, and K. L. Polzin, 2013a: Sensitivity of the ocean state to the vertical distribution of internal-tide-driven mixing. *J. Phys. Oceanogr.*, **43**, 602–615, doi:10.1175/JPO-D-12-055.1.

——, M. Nikurashin, C. J. Muller, S. Falahat, J. Nycander, P. G. Timko, B. K. Arbic, and J. A. Goff, 2013b: Internal tide generation by abyssal hills using analytical theory. *J. Geophys. Res. Oceans*, **118**, 6303–6318, doi:10.1002/2013JC009212.

——, R. Hallberg, S. Legg, and M. Nikurashin, 2014: Sensitivity of the ocean state to lee wave–driven mixing. *J. Phys. Oceanogr.*, **44**, 900–921, doi:10.1175/JPO-D-13-072.1.

Morozov, E. G., 1995: Semidiurnal internal wave global field. *Deep-Sea Res. I*, **42**, 135–148, doi:10.1016/0967-0637(95)92886-C.

Moum, J. N., D. R. Caldwell, J. D. Nash, and G. D. Gunderson, 2002: Observations of boundary mixing over the continental slope. *J. Phys. Oceanogr.*, **32**, 2113–2130, doi:10.1175/1520-0485(2002)032<2113:OOBMOT>2.0.CO;2.

Müller, P., and N. Xu, 1992: Scattering of oceanic internal gravity waves off random bottom topography. *J. Phys. Oceanogr.*, **22**, 474–488, doi:10.1175/1520-0485(1992)022<0474:SOOIGW>2.0.CO;2.

Munk, W., and C. Wunsch, 1998: Abyssal recipes II: Energetics of tidal and wind mixing. *Deep-Sea Res.*, **45**, 1977–2010, doi:10.1016/S0967-0637(98)00070-3.

Nash, J. D., J. M. Kunze, E. Toole, and R. W. Schmitt, 2004: Internal tide reflection and turbulent mixing on the continental slope. *J. Phys. Oceanogr.*, **34**, 1117–1134, doi:10.1175/1520-0485(2004)034<1117:ITRATM>2.0.CO;2.

——, M. H. Alford, E. Kunze, K. Martini, and S. Kelly, 2007: Hotspots of deep ocean mixing on the Oregon continental slope. *Geophys. Res. Lett.*, **34**, L01605, doi:10.1029/2006GL028170.

——, S. M. Kelly, E. L. Shroyer, J. N. Moum, and T. F. Duda, 2012: The unpredictable nature of internal tides on continental shelves. *J. Phys. Oceanogr.*, **42**, 1981–2000, doi:10.1175/JPO-D-12-028.1.

Nikurashin, M., and R. Ferrari, 2011: Global energy conversion rate from geostrophic flows into internal lee waves in the deep ocean. *Geophys. Res. Lett.*, **38**, L08610, doi:10.1029/2011GL046576.

——, and S. Legg, 2011: A mechanism for local dissipation of internal tides generated at rough topography. *J. Phys. Oceanogr.*, **41**, 378–395, doi:10.1175/2010JPO4522.1.

Nycander, J., 2005: Generation of internal waves in the deep ocean by tides. *J. Geophys. Res.*, **110**, C10028, doi:10.1029/2004JC002487.

Oakey, N. S., 1982: Determination of the rate of dissipation of turbulent energy from simultaneous temperature and velocity shear microstructure measurements. *J. Phys. Oceanogr.*, **12**, 256–271, doi:10.1175/1520-0485(1982)012<0256:DOTROD>2.0.CO;2.

Oka, A., and Y. Niwa, 2013: Pacific deep circulation and ventilation controlled by tidal mixing away from the sea bottom. *Nat. Commun.*, **4**, 2419, doi:10.1038/ncomms3419.

Osborn, T. R., 1980: Estimates of the local rate of vertical diffusion from dissipation measurements. *J. Phys. Oceanogr.*, **10**, 83–89, doi:10.1175/1520-0485(1980)010<0083:EOTLRO>2.0.CO;2.

Park, Y.-G., and K. Bryan, 2000: Comparison of thermally driven circulations from a depth-coordinate model and an isopycnal-layer model. Part I: Scaling-law sensitivity to vertical diffusivity. *J. Phys. Oceanogr.*, **30**, 590–605, doi:10.1175/1520-0485(2000)030<0590:COTDCF>2.0.CO;2.

Polzin, K. L., 2004: Idealized solutions for the energy balance of the finescale internal wave field. *J. Phys. Oceanogr.*, **34**, 231–246, doi:10.1175/1520-0485(2004)034<0231:ISFTEB>2.0.CO;2.

——, 2008: Mesoscale eddy–internal wave coupling. Part I: Symmetry, wave capture, and results from the Mid-Ocean Dynamics Experiment. *J. Phys. Oceanogr.*, **38**, 2556–2574, doi:10.1175/2008JPO3666.1.

——, 2009: An abyssal recipe. *Ocean Modell.*, **30**, 298–309, doi:10.1016/j.ocemod.2009.07.006.

——, J. M. Toole, and R. W. Schmitt, 1995: Finescale parameterizations of turbulent dissipation. *J. Phys. Oceanogr.*, **25**, 306–328, doi:10.1175/1520-0485(1995)025<0306:FPOTD>2.0.CO;2.

——, ——, J. R. Ledwell, and R. W. Schmitt, 1997: Spatial variability of turbulent mixing in the abyssal ocean. *Science*, **276**, 93–96, doi:10.1126/science.276.5309.93.

Rainville, L. N., and R. Pinkel, 2006: Baroclinic energy flux at the Hawaiian Ridge: Observations from the R/P *FLIP*. *J. Phys. Oceanogr.*, **36**, 1104–1122, doi:10.1175/JPO2882.1.

Ray, R., and G. Mitchum, 1997: Surface manifestation of internal tides in the deep ocean: Observations from altimetry and island gauges. *Prog. Oceanogr.*, **40**, 135–162, doi:10.1016/S0079-6611(97)00025-6.

Rudnick, D. L., and Coauthors, 2003: From tides to mixing along the Hawaiian Ridge. *Science*, **301**, 355–357, doi:10.1126/science.1085837.

Saenko, O. A., and W. J. Merryfield, 2005: On the effect of topographically enhanced mixing on the global ocean circulation. *J. Phys. Oceanogr.*, **35**, 826–834, doi:10.1175/JPO2722.1.

——, X. Zhai, W. J. Merryfield, and W. G. Lee, 2012: The combined effect of tidally and eddy driven diapycnal mixing on the large-scale ocean circulation. *J. Phys. Oceanogr.*, **42**, 526–538, doi:10.1175/JPO-D-11-0122.1.

Schiermeier, Q., 2007: Churn, churn, churn. *Nature*, **447**, 522–524, doi:10.1038/447522a.

Scott, J. R., and J. Marotzke, 2002: The location of diapycnal mixing and the meridional overturning circulation. *J. Phys. Oceanogr.*, **32**, 3578–3595, doi:10.1175/1520-0485(2002)032<3578:TLODMA>2.0.CO;2.

Scott, R. B., J. A. Goff, A. C. Naveira Garabato, and A. J. Nurser, 2011: Global rate and spectral characteristics of internal gravity wave generation by geostrophic flow over topography. *J. Geophys. Res.*, **116**, C09029, doi:10.1029/2011JC007005.

Simmons, H. L., R. W. Hallberg, and B. K. Arbic, 2004a: Internal wave generation in a global baroclinic tide model. *Deep-Sea Res. II*, **51**, 3043–3068, doi:10.1016/j.dsr2.2004.09.015.

——, S. R. Jayne, L. C. St. Laurent, and A. J. Weaver, 2004b: Tidally driven mixing in a numerical model of the ocean general circulation. *Ocean Modell.*, **6**, 245–263, doi:10.1016/S1463-5003(03)00011-8.

Smith, W. H. F., and D. T. Sandwell, 1997: Global sea floor topography from satellite altimetry and ship depth soundings. *Science*, **277**, 1956–1962, doi:10.1126/science.277.5334.1956.

Sokolov, A. P., C. E. Forest, and P. H. Stone, 2003: Comparing oceanic heat uptake in AOGCM transient climate change experiments. *J. Climate*, **16**, 1573–1582, doi:10.1175/1520-0442-16.10.1573.

St. Laurent, L. C., and R. W. Schmitt, 1999: The contribution of salt fingers to vertical mixing in the North Atlantic Tracer Release Experiment. *J. Phys. Oceanogr.*, **29**, 1404–1424, doi:10.1175/1520-0485(1999)029<1404:TCOSFT>2.0.CO;2.

——, H. L. Simmons, and S. R. Jayne, 2002: Estimating tidally driven mixing in the deep ocean. *Geophys. Res. Lett.*, **29**, 2106, doi:10.1029/2002GL015633.

Thiele, G., and J. L. Sarmiento, 1990: Tracer dating and ocean ventilation. *J. Geophys. Res.*, **95**, 9377–9391, doi:10.1029/JC095iC06p09377.

Thurnherr, A. M., L. C. St. Laurent, K. G. Speer, J. M. Toole, and J. R. Ledwell, 2005: Mixing associated with sills in a canyon on the midocean ridge flank. *J. Phys. Oceanogr.*, **35**, 1370–1381, doi:10.1175/JPO2773.1.

Toole, J. M., R. W. Schmitt, K. L. Polzin, and E. Kunze, 1997: Near-boundary mixing above the flanks of a midlatitude seamount. *J. Geophys. Res.*, **102**, 947–959, doi:10.1029/96JC03160.

Waterhouse, A., and Coauthors, 2014: Global patterns of diapycnal mixing from measurements of the turbulent dissipation rate. *J. Phys. Oceanogr.*, **44**, 1854–1872, doi:10.1175/JPO-D-13-0104.1.

Wunsch, C., and R. Ferrari, 2004: Vertical mixing, energy and the general circulation of the oceans. *Annu. Rev. Fluid Mech.*, **36**, 281–314, doi:10.1146/annurev.fluid.36.050802.122121.

Zhao, Z., M. H. Alford, and J. B. Girton, 2012: Mapping low-mode internal tides from multisatellite altimetry. *Oceanography*, **25** (2), 42–51, doi:10.5670/oceanog.2012.40.